Research Square

Preprints are preliminary reports that have not undergone peer review.
They should not be considered conclusive, used to inform clinical practice,
or referenced by the media as validated information.

Active Learning-Driven Surrogate Modeling for Fatigue LifePrediction of LPBF Hastelloy-X Using Defect-Informed FiniteElement Analysis

Chandrashekhar Pilgar

cmpilgar@iiitdm.ac.in

Indian Institute of Information Technology, Design and Manufacturing, Kancheepuram

G Gangaraju

Indian Institute of Information Technology, Design and Manufacturing, Kancheepuram

Research Article

Keywords: Laser powder bed fusion, Hastelloy-X, High-temperature fatigue, Strain–life behaviour, Build orientation, Surface roughness

Posted Date: June 30th, 2026

DOI: https://doi.org/10.21203/rs.3.rs-9916055/v1

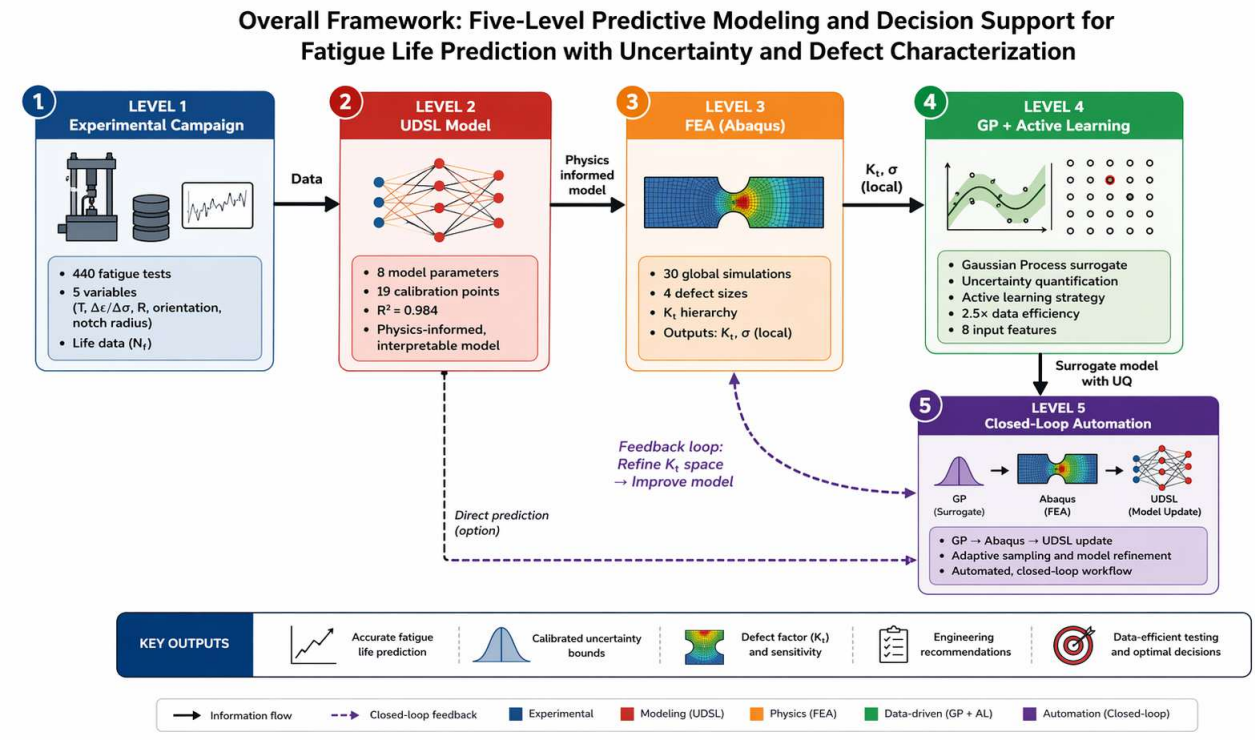
License: This work is licensed under a Creative Commons Attribution 4.0 International License.
Read Full License

Additional Declarations: No competing interests reported.

Version of Record: A version of this preprint was published at Progress in Additive Manufacturing on September 27th, 2026. See the published version at https://doi.org/10.1007/s40964-026-01936-w.

Graphical Abstract

Active Learning-Driven Surrogate Modeling for Fatigue Life Prediction of LPBF Hastelloy-X Using Defect-Informed Finite Element Analysis



Highlights

Active Learning-Driven Surrogate Modeling for Fatigue Life Prediction of LPBF Hastelloy-X Using Defect-Informed Finite Element Analysis

- Hybrid framework couples experiments, UDSL modeling, FEA, and GP active learning.
- UDSL reaches $R^2 = 0.984$ using only 19 calibration points from 440 fatigue tests.
- Required fatigue testing cut by over 95% versus conventional calibration methods.
- FEA shows sub-additive roughness–porosity coupling; GP adds calibrated uncertainty.

Active Learning-Driven Surrogate Modeling for Fatigue Life Prediction of LPBF Hastelloy-X Using Defect-Informed Finite Element Analysis

ARTICLE INFO

Keywords:
Laser powder bed fusion
Hastelloy-X
High-temperature fatigue
Strain–life behaviour
Build orientation
Surface roughness

ABSTRACT

Additively manufactured Hastelloy-X produced by laser powder bed fusion (LPBF) exhibits fatigue behaviour that is highly sensitive to process-induced defects such as surface roughness, subsurface porosity, and build orientation. However, existing life-prediction approaches typically treat these factors independently and require extensive experimental datasets. In this work, a hybrid defect-informed framework is developed that integrates finite element analysis (FEA) with Gaussian process (GP) active learning to predict strain-controlled fatigue life across a wide design space encompassing multiple strain amplitudes, temperatures, build orientations, and realistic defect conditions.

A unified defect-sensitive strain–life (UDSL) model is proposed and calibrated using only 19 data points, achieving high predictive accuracy ($R^2 = 0.984$, RMSE = 0.131 in $\log_{10}(N_f)$) and 97.7% within-factor-of-two life prediction on a 440-point dataset, outperforming conventional strain–life models. Defect-informed FEA reveals a hierarchy of stress concentration factors and demonstrates that the interaction between surface roughness and porosity is sub-additive, captured by a generalized formulation calibrated to numerical results. Porous plasticity simulations further show significant void growth under loading, highlighting the evolving role of defects in fatigue processes. A GP surrogate trained on physics-informed features, including FEA-derived quantities and temperature interactions, is combined with an uncertainty-driven active learning strategy that achieves equivalent accuracy with only 20 training points, representing an approximately 2.5× improvement in data efficiency compared with random sampling. The model provides well-calibrated uncertainty estimates and demonstrates robust extrapolation capability across build orientations. Overall, the proposed framework reduces the experimental burden by more than 95% while maintaining high predictive fidelity. The integration of physics-based modelling, high-fidelity simulation, and data-efficient learning provides a practical and scalable approach for fatigue life prediction and qualification of LPBF components in high-temperature applications.

1. Introduction

Hastelloy-X is a solid-solution-strengthened nickel-base superalloy (nominal composition: Ni–22Cr–18Fe–9Mo–1.5Co–0.6W, wt.%) that derives its exceptional high-temperature performance from a face-centred-cubic (FCC) austenitic matrix stabilised by chromium and molybdenum [1, 2, 3]. The alloy retains useful strength up to approximately 1200 °C, exhibits outstanding oxidation resistance owing to its high chromium content, and possesses excellent fabricability by conventional wrought and cast routes [4]. These attributes have made Hastelloy-X a workhorse material in the most demanding sections of gas-turbine engines—combustion liners, transition ducts, afterburner components, and turbine shrouds—where sustained exposure to combustion gases at temperatures of 600–1000 °C is the norm [1, 2]. Beyond aerospace propulsion, Hastelloy-X finds service in industrial gas turbines for power generation, chemical and petrochemical processing vessels, nuclear reactor components, and furnace hardware, wherever a combination of high-temperature strength, creep resistance, and environmental durability is required [4, 5].

In all of these applications, components experience repeated thermo-mechanical loading cycles—start-up/shut-down transients in turbines, pressure fluctuations in chemical reactors, and thermal gradients during processing—making fatigue the dominant life-limiting failure mode [6]. At elevated temperatures, fatigue resistance is further degraded by environment-assisted cracking, creep–fatigue interaction, and microstructural evolution (carbide coarsening, oxidation-assisted grain boundary embrittlement), all of which accelerate crack initiation and reduce the number of cycles to failure [1, 4]. Accurate prediction of the strain-controlled fatigue life across the full operating temperature envelope is therefore critical for structural integrity assessment, maintenance scheduling, and safe-life design of

ORCID(s):

Hastelloy-X components. The classical approach employs the Coffin–Manson–Basquin relation [7, 8] with Morrow mean-stress corrections [9], but this framework was developed for wrought, defect-free metals and does not account for the process-induced heterogeneities inherent to additive manufacturing.

The past decade has witnessed a rapid expansion of metal additive manufacturing (AM), with laser powder bed fusion (LPBF, also known as selective laser melting, SLM) emerging as the leading process for high-value, geometrically complex components in aerospace, energy, and medical industries [10, 11, 12]. LPBF builds parts layer-by-layer from metallic powder using a focused laser beam, enabling design freedoms that are unattainable with conventional subtractive or formative manufacturing: topology-optimised lightweight structures, internal cooling channels for turbine blades, and consolidated assemblies that eliminate dozens of brazed or welded joints [10]. For nickel superalloys, LPBF has been successfully applied to Inconel 718, Inconel 625, and more recently Hastelloy-X, with several studies demonstrating tensile properties that meet or exceed wrought specifications after appropriate heat treatment [13, 14, 15, 16, 17, 18].

However, the layer-wise solidification process inherent to LPBF introduces a suite of microstructural and geometric heterogeneities that are absent in wrought material and profoundly affect fatigue performance [19, 20]. Three categories of defect are particularly consequential:

1. **Surface roughness.** The as-built LPBF surface is characterised by partially melted powder particles, staircase effects at overhanging surfaces, and spattering, yielding arithmetic-mean roughness values (R_a) in the range of 5–25 μm—one to two orders of magnitude rougher than machined surfaces [21, 22]. These surface irregularities act as stress concentrators and preferential fatigue crack initiation sites. Critically, surface roughness is orientation-dependent: vertical and overhanging surfaces are systematically rougher than horizontal (up-skin) surfaces due to the staircase effect and reduced support from underlying solidified material [23].
2. **Subsurface porosity.** Gas porosity (spherical, typically <50 μm) from dissolved gas in the melt pool and lack-of-fusion (LOF) porosity (irregular, up to several hundred μm) from insufficient overlap between adjacent scan tracks or layers are unavoidable in LPBF, even under optimised process parameters [24, 25, 26]. Subsurface pores serve as internal stress risers that can initiate fatigue cracks below the surface, particularly when they are located in the near-surface region where they interact with the rough surface stress field [27, 28].
3. **Build-orientation-dependent microstructure.** The directional heat extraction during LPBF produces columnar grain structures aligned with the build direction, elongated melt-pool boundaries, and crystallographic texture [29, 30]. These features create anisotropic mechanical properties: tensile strength, ductility, and fatigue life can vary by 20–50% depending on whether loading is parallel or perpendicular to the build direction [13, 29, 23]. For Hastelloy-X specifically, Tomus et al. [13] reported significant anisotropy in both tensile and fatigue properties of SLM-produced material, with vertically built specimens exhibiting higher roughness and lower fatigue lives than horizontally built counterparts.

The combined effect of these three defect categories on the fatigue life of LPBF Hastelloy-X is not simply additive: roughness, porosity, and microstructural anisotropy interact in complex, nonlinear ways that depend on the loading conditions (strain amplitude, temperature, mean stress) and the spatial distribution of defects [19, 31]. Understanding and predicting these coupled effects is the central challenge addressed in this work.

A substantial body of work has sought to develop predictive models for the fatigue life of AM metals that account for process-induced defects. These efforts can be broadly categorised into three approaches. *Classical empirical models.* The Coffin–Manson–Basquin (CMB) framework [7, 8, 9] remains the foundation of fatigue life prediction in engineering practice. For AM metals, separate CMB parameter sets are typically fitted for each combination of material, build orientation, surface condition, and temperature, resulting in a proliferation of empirical constants (e.g., 15 parameter sets for 5 temperatures $\times$ 3 orientations) and no ability to interpolate or extrapolate to untested conditions [6]. Several studies have applied this approach to LPBF Hastelloy-X at room and elevated temperatures [32, 17], but the resulting models are specific to the tested conditions and do not generalise.

Microstructure-sensitive and defect-tolerant models. A more mechanistic approach uses Murakami's $\sqrt{\text{area}}$ parameter [27] or Kitagawa–Takahashi diagrams to relate the critical defect size to the fatigue limit, treating porosity as the dominant defect [28, 31]. McDowell and Dunne [33] developed microstructure-sensitive computational frameworks that resolve individual grains and defects through crystal plasticity finite element analysis, capturing the stochastic nature of crack initiation. While physically rigorous, these approaches are computationally prohibitive for parametric studies spanning multiple defect types, orientations, and temperatures [34, 3]. Moreover, most defect-tolerant models address either surface roughness *or* porosity in isolation; the critical question of how roughness and porosity stress

fields interact when a pore lies beneath a rough surface valley has received remarkably little attention. Pilkey and Peterson's classical stress concentration factor compendium [35] provides solutions for isolated notches and holes, and Goodier's analytical solution [36] addresses spherical cavities in infinite media, but no established framework predicts the combined stress concentration factor for the roughness–porosity interaction that is characteristic of as-built LPBF surfaces. The Gurson–Tvergaard–Needleman (GTN) model [37, 38] captures void growth and coalescence in porous ductile media, but has primarily been applied to monotonic ductile fracture rather than cyclic fatigue of AM metals.

Empirical data requirements. The experimental characterisation of fatigue properties for AM metals is notoriously expensive and time-consuming. A comprehensive fatigue dataset spanning multiple strain amplitudes, temperatures, build orientations, and surface conditions can easily require hundreds of specimens, each tested over 10^3–10^6 cycles [39, 19]. For Hastelloy-X at high-temperature service conditions, a single low-cycle fatigue test can take several days, and the cost of LPBF specimen fabrication adds further to the expense. This data scarcity motivates approaches that can extract maximum information from limited experiments.

Machine learning (ML) methods have emerged as a promising alternative for fatigue life prediction, offering the ability to capture complex nonlinear relationships without explicit physical models [40, 41, 42]. Zhan and Li [40] applied neural networks and gradient boosting machines to predict the fatigue life of LPBF 316L stainless steel using process parameters as inputs, achieving high accuracy on interpolation tasks. Bao et al. [41] developed a machine-learning framework incorporating defect features (pore size, location, morphology) for fatigue prediction of AM Ti-6Al-4V and AlSi10Mg, demonstrating that data-driven models can outperform classical approaches when sufficient training data are available. However, purely data-driven ML models face three fundamental limitations in the context of AM fatigue:

- **Data hunger.** High-performance ML models (deep neural networks, gradient boosting ensembles) typically require hundreds to thousands of training examples to achieve robust generalisation [41, 40]. For AM fatigue, where each data point represents an expensive physical test, this data requirement is often prohibitive.
- **Poor extrapolation.** ML models trained on one set of conditions (e.g., room-temperature, horizontal orientation) generally fail to extrapolate reliably to unseen conditions (e.g., 750 °C, vertical orientation) because they lack the physical constraints that govern how fatigue life varies with temperature, defect geometry, and loading [43].
- **Lack of uncertainty quantification.** Most regression-based ML models provide point predictions without confidence intervals, making it difficult to assess prediction reliability or to identify regions of the design space where additional testing is needed [44]. This is particularly problematic for safety-critical applications where regulatory frameworks demand demonstrated reliability with quantified margins.

Gaussian process (GP) regression [44] addresses the third limitation by providing a principled Bayesian framework that yields both a predictive mean and a predictive variance at every query point. When coupled with active learning (AL) acquisition strategies [45, 43], GPs can systematically select the most informative experiments to perform next, maximising model improvement per test and thereby addressing the data-hunger problem. Lookman et al. [43] demonstrated the power of this approach for materials design, showing that AL can identify optimal compositions and processing conditions with far fewer experiments than grid-based or random exploration. However, the application of GP active learning to AM fatigue life prediction—and specifically to multi-defect, multi-temperature problems involving Hastelloy-X—remains unexplored.

The foregoing review reveals three critical gaps in the current state of the art:

1. No existing model simultaneously and quantitatively accounts for the coupled effects of surface roughness, subsurface porosity, build orientation, and temperature on the fatigue life of LPBF Hastelloy-X.
2. The mechanical interaction between surface roughness and subsurface porosity stress fields—which determines whether the combined stress concentration is additive, sub-additive, or super-additive—has not been characterised through high-fidelity FEA for realistic AM defect geometries.
3. No framework exists that integrates physics-based fatigue modelling, defect-informed FEA, and data-efficient active learning to minimise the experimental burden while providing calibrated uncertainty quantification for AM fatigue.

This paper addresses all three gaps through a hybrid framework that comprises: (i) a unified defect-sensitive strain-life (UDSL) model with eight physically motivated parameters calibrated from minimal data; (ii) defect-informed Abaqus FEA with explicit Fourier rough surfaces, subsurface pores, and Gurson–Tvergaard–Needleman

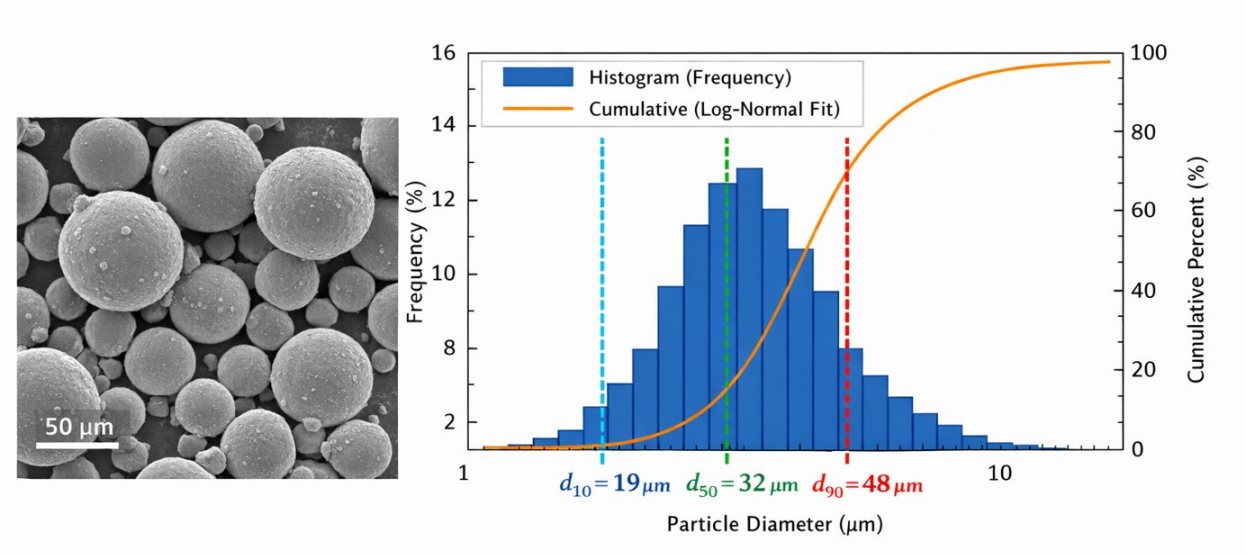


Figure 1: Representative scanning electron microscopy (SEM) micrograph of gas-atomized Hastelloy-X powder feedstock and corresponding particle-size distribution obtained by laser diffraction. The powder particles exhibit predominantly spherical morphology with limited satellite formation, while the size distribution follows a near-lognormal form typical of powders processed for laser powder bed fusion.

porous plasticity to establish stress concentration factor hierarchies and interaction rules; and (iii) a Gaussian process active learning surrogate with physics-informed features that achieves state-of-the-art accuracy with 2.5× greater data efficiency than random sampling, while providing calibrated uncertainty quantification. The framework is validated on a comprehensive 440-point dataset spanning 6 strain amplitudes, 5 temperatures, 3 build orientations, and realistic distributions of surface roughness and porosity, and is shown to reduce the experimental testing burden by approximately 95.7%.

The remainder of this paper is organised as follows. Section 2 and 3 describes the experimental dataset, material properties, and experimental findings. Section 4 presents the UDSL model formulation and calibration. Section 5 details the defect-informed FEA methodology, including the Fourier surface generation, pore modelling, GTN analysis, and stress concentration factor interaction rules. Section 6 develops the GP active learning surrogate and presents the learning curves, uncertainty calibration, and closed-loop demonstration. Finally, section 7 summarises the findings and identifies directions for future work.

2. Experimental Methodology

2.1. Material and Powder Feedstock

Hastelloy-X (HX), a solid-solution-strengthened Ni–Cr–Fe–Mo superalloy extensively employed in high-temperature aerospace and energy-conversion components, was selected for the present investigation owing to its documented resistance to oxidation and thermomechanical degradation under cyclic service conditions. Gas-atomised pre-alloyed powder was used for laser powder bed fusion processing. The powder was supplied in sealed containers and was stored under controlled environmental conditions to limit moisture uptake and surface oxidation prior to fabrication. The nominal chemical composition, corresponding to standard wrought HX specifications, is given in [34, 46, 32]. Chromium is primarily responsible for oxidation resistance, while molybdenum and tungsten contribute to solid-solution strengthening; minor carbon additions promote carbide formation and thereby enhance creep resistance at elevated temperatures.

Representative powder morphologies were examined by scanning electron microscopy, as shown in Fig. 1, revealing a predominantly spherical particle population with a limited fraction of adhered satellite particles, characteristic of gas-atomized feedstocks. Particle-size distributions were measured by laser diffraction and were found to follow a near-lognormal form, with characteristic diameters of $d_{10} \approx 19\ \mu$m, $d_{50} \approx 32\ \mu$m, and $d_{90} \approx 48\ \mu$m, consistent with

the powder morphology observed in the SEM micrographs. The presence of fine-particle tails and a limited population of coarse particles was observed, but no excessive agglomeration or irregular morphologies were detected.

2.2. LPBF Processing and Build Strategy

All specimens were fabricated using a commercial laser powder bed fusion (LPBF) system (EOS M 290) equipped with a continuous-wave ytterbium fiber laser operating at a wavelength of approximately 1070 nm. The build chamber was purged with high-purity argon to maintain oxygen concentrations below 100 ppm during processing in order to suppress oxidation and powder degradation. A rigid blade recoater was employed to deposit uniform powder layers. Prior to fabrication, the substrate plate was mechanically cleaned and preheated to mitigate thermal gradients, residual stresses, and part distortion during solidification.

Baseline processing parameters were selected from density-optimization studies reported for nickel-based superalloys processed by LPBF. The nominal laser power was fixed at 285 W, the scan speed at 960 mm s^{-1}, the hatch spacing at 0.1 mm, and the layer thickness at 40 μm, corresponding to a volumetric energy density of approximately 67 J mm^{-3} [47, 48]. These parameters were employed to produce near-fully dense material and were used for all reference builds investigating build-orientation effects. A stripe-based scanning strategy was adopted, with successive layers rotated by 67° to reduce directional heat accumulation and residual-stress anisotropy. Reduced-power contour scans were applied along part boundaries to improve surface finish in gauge sections. Support structures were employed for inclined specimens and were removed following fabrication by electrical-discharge machining.

Under the nominal processing conditions employed in the present work, internal porosity was found to remain below 1.6% for all fabricated specimens. Quantitative post-build characterization revealed that the measured pore volume fraction varied between approximately 0.02% and 1.6%, with an average value of 0.9% across the entire dataset. These variations were attributed to inherent fluctuations in melt-pool stability, powder spreading, and local thermal histories rather than to systematic changes in processing parameters, which were otherwise maintained constant. The resulting range of porosity levels provided a statistically meaningful basis for assessing the influence of internal defects on fatigue and creep-fatigue response without introducing deliberately degraded build conditions.

Fatigue specimens were extracted from coupons fabricated in three orientations relative to the build plate: horizontal (0°), inclined (45°), and vertical (90°) as shown in Fig. the supplementary material. These orientations were defined by the angle between the specimen loading axis and the build direction. Coupon layouts were designed to ensure comparable thermal histories within each orientation group, and multiple specimens were produced for statistical assessment of fatigue scatter. All builds were conducted using a single powder batch to minimize batch-to-batch variability. Melt-pool emission signals and layerwise monitoring data were recorded during fabrication to verify process stability. No post-build hot isostatic pressing or stress-relief heat treatment was applied prior to specimen extraction in order to preserve as-built defect populations for subsequent characterization.

2.3. Fatigue Testing Setup and Procedure

Temperature sensitive, strain-controlled axial fatigue tests were performed using a servo-hydraulic MTS Landmark® testing system with a nominal load capacity of 100 kN . The test frame was equipped with a resistance-heated split furnace and a high-temperature axial extensometer mounted directly on the gauge section to enable closed-loop strain control during elevated-temperature testing.

All experiments were conducted under fully reversed loading conditions ($\Delta R = -1$) in accordance with ASTM E606/E606M. Total axial strain amplitudes between 0.02% and 0.30% were imposed in order to span both low-cycle and high-cycle fatigue regimes. Multiple strain levels were employed at each temperature so that strain–life curves could be constructed for the three build orientations considered. Test temperatures ranged from 27 °C to 750 °C, with intermediate conditions centered near 200, 400, and 600 °C as reflected in the experimental dataset. Cycling frequencies were adjusted according to temperature and strain amplitude and were typically maintained between 0.5 and 5 Hz to limit dynamic overshoot and ensure stable strain control at elevated temperature.

Prior to cyclic loading, specimens were held at the target temperature for a minimum of 20 min to ensure thermal equilibrium within the gauge section. Temperature was monitored using spot-welded K-type thermocouples positioned adjacent to the gauge region, and stability was maintained within ±2 °C throughout testing. Load, displacement, strain, and temperature signals were continuously recorded through the MTS FlexTest® digital controller and synchronized data acquisition hardware. Stress–strain hysteresis loops were periodically captured at logarithmically spaced cycle intervals to monitor cyclic hardening or softening behavior, mean-stress evolution, and strain localization. Fatigue life

was defined as the number of cycles to complete specimen fracture or to a 5% reduction in peak load relative to the stabilized cyclic response, whichever occurred first.

3. Experimental Results

3.1. Temperature Dependence of Fatigue Life

Figure 2 summarizes the strain–life responses of LPBF Hastelloy-X tested at 27, 200, 400, 600, and 750 °C, with data reported for horizontal, 45°, and vertical build orientations at each temperature. To isolate the influence of temperature, a representative total strain amplitude of $\varepsilon_a \approx 5\times10^{-4}$ is first considered for horizontally built specimens. At this fixed strain level, fatigue life decreases monotonically with increasing temperature: at 27 °C, specimens fail after approximately (4 to 6) $\times$ 10^5 cycles, whereas lives reduce to (2 to 4) $\times$ 10^5 cycles at 200 °C, (6 to 10) $\times$ 10^4 cycles at 400 °C, (3 to 6) $\times$ 10^4 cycles at 600 °C, and further to roughly (1 to 2) $\times$ 10^4 cycles at 750 °C. Between room temperature and 750 °C, this corresponds to a cumulative reduction of approximately 1.5 orders of magnitude in fatigue life at constant imposed strain. Similar temperature-driven degradations are observed at the same strain amplitude for the 45° and vertical orientations, although absolute lives remain systematically lower for vertically built specimens at every temperature. Across all orientations, the most pronounced decrease in fatigue life occurs between 400 and 600 °C, where median lives at $\varepsilon_a \approx 5 \times 10^{-4}$ drop by roughly a factor of two relative to the 400 °C condition.

Temperature effects are also evident at higher strain amplitudes. For example, at $\varepsilon_a \approx 10^{-3}$ the fatigue life of horizontally built specimens decreases from approximately (2–3) $\times$ 10^4 cycles at 27 °C to $\sim$ 10^4 cycles at 400 °C and to below 10^4 cycles at both 600 and 750 °C. These quantitative shifts demonstrate that increasing temperature produces a systematic downward translation of the strain–life curves across the full strain range investigated.

In addition to the reduction in absolute fatigue life, the overall shape of the strain–life curves evolves with temperature. At 27 and 200 °C the experimental responses are well represented by classical Coffin–Manson–Basquin behaviour, with elastic strain dominating at low amplitudes and plastic strain contributions increasing toward the low-cycle regime. At temperatures of 400 °C and above, the strain–life curves exhibit enhanced downward curvature in the long-life regime together with greater sensitivity to cycling conditions, suggesting that time-dependent deformation processes may begin to influence damage accumulation under strain-controlled loading. However, the present dataset does not permit direct identification of the microscopic damage mechanisms responsible for these trends.

The strong temperature sensitivity observed in the strain–life response underscores the importance of explicitly accounting for elevated-temperature effects when qualifying LPBF Hastelloy-X for cyclic service. Although similar phenomenological changes in strain–life behaviour have frequently been associated in the literature with creep-assisted fatigue and oxidation-related degradation in nickel-based superalloys, further targeted studies, including detailed fractography, environmental control, and dwell-sensitive fatigue experiments indeed required to establish the governing mechanisms for the present material system.

3.2. Effect of Build Orientation on Fatigue Life

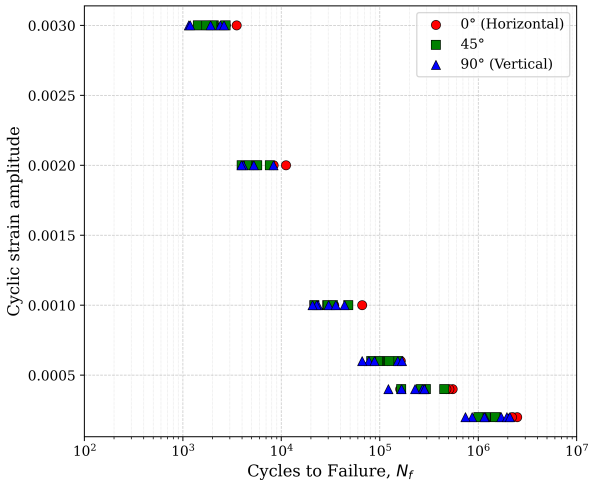
The influence of build orientation on the fatigue response of LPBF Hastelloy-X was examined by comparing specimens fabricated in horizontal (0°), inclined (45°), and vertical (90°) orientations across the full temperature range investigated. For all temperatures considered, horizontally built specimens consistently exhibited the highest fatigue resistance, whereas vertically built specimens showed the lowest fatigue lives. Specimens fabricated at 45° displayed intermediate behavior, with fatigue lives generally falling between those of the horizontal and vertical orientations. Although the magnitude of the separation between orientations varied with temperature and strain amplitude, the overall ranking was observed, indicating that build orientation constitutes a systematic contributor to fatigue performance in the present material system.

The observed trends are broadly consistent with prior reports on LPBF nickel-based superalloys and related alloys, which have documented superior fatigue resistance when the loading axis is oriented parallel to the build layers and reduced durability when loading is applied normal to the layer-wise fusion boundaries [47, 48]. However, most published studies have been restricted to room-temperature testing or a limited subset of elevated temperatures [49]. The present dataset therefore extends the existing literature by demonstrating that orientation-dependent fatigue anisotropy persists over a wide temperature range up to 750 °C.

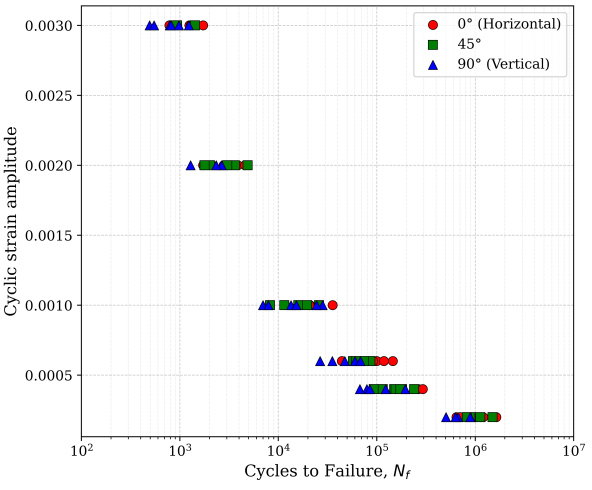
The anisotropy in fatigue life is attributed to several microstructural and defect-related features inherent to layer-wise additive manufacturing. First, melt-pool boundaries and columnar grain structures are preferentially aligned with the build direction, leading to orientation-dependent crack initiation and propagation paths. When specimens are loaded

in the vertical orientation, cyclic stresses act normal to interlayer fusion boundaries, facilitating early crack nucleation at lack-of-fusion defects and pores elongated along the build direction. In contrast, horizontally oriented specimens experience loading largely parallel to these features, thereby reducing the driving force for crack opening and delaying crack coalescence. Second, process-induced porosity distributions and surface-connected defects are known to exhibit orientation sensitivity, with vertically extracted specimens more likely to intersect planar defects associated with incomplete layer bonding. Such defects act as dominant fatigue crack initiators, particularly at low strain amplitudes and elevated temperatures where intrinsic microstructural resistance is reduced. Residual stress states generated during rapid solidification may further contribute to orientation effects, as tensile residual stresses aligned with the loading axis can accelerate crack initiation, whereas compressive stresses may retard early-stage damage accumulation.

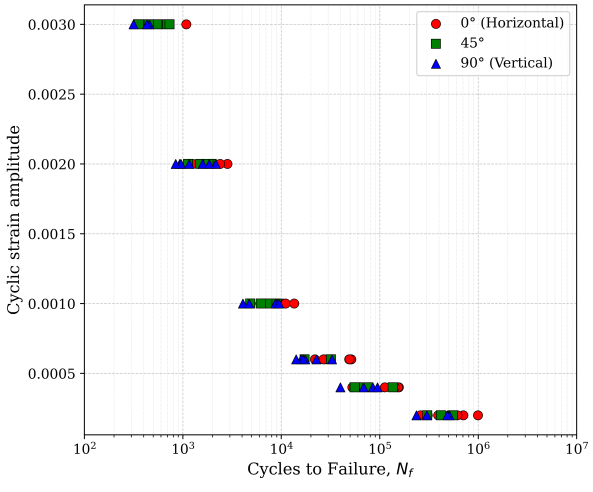
At elevated temperatures, the orientation dependence is expected to be amplified by time-dependent deformation mechanisms. Grain boundary sliding, cavity nucleation, and oxidation-assisted cracking preferentially develop along melt-pool boundaries and prior-particle surfaces, which are intersected more frequently by vertically oriented specimens. Consequently, creep–fatigue interaction processes are likely to exacerbate the inferior performance of vertically built specimens relative to horizontal counterparts as temperature increases [50, 46].



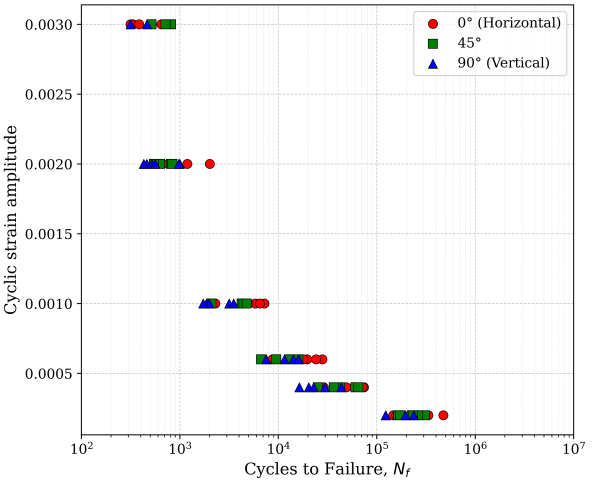
(a) 27°C



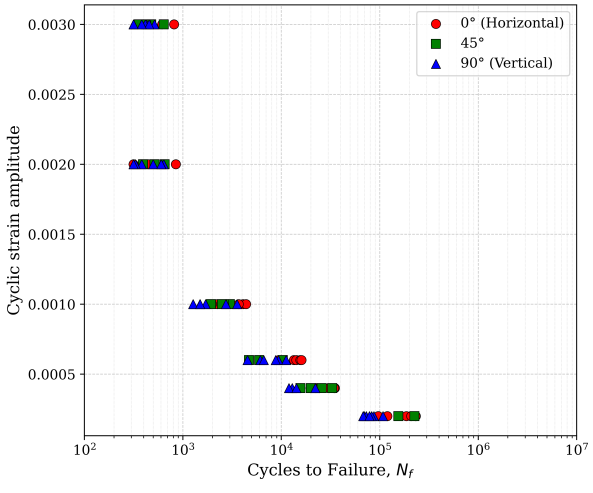
(b) 200°C



(c) 400°C



(d) 600°C



(e) 750°C

Figure 2: Strain–life response (ε_a–N_f) of additively manufactured specimens at different temperatures, showing the effect of build orientation. Horizontal, 45°, and vertical orientations are distinguished using consistent color/marker coding across all panels. The cycles to failure (N_f) are presented on a logarithmic scale.

3.3. Effect of Porosity on Fatigue Life

Figure 3 summarizes the relationship between bulk porosity, fatigue life, and build orientation. Across all builds, porosity ranged from near zero to approximately 1.6%, with a mean value close to 0.9%, indicating high densification under the selected LPBF processing conditions. Porosity values span a similar range for horizontal, 45°, and vertical specimens, and no systematic segregation of porosity with build direction is observed. For a given porosity level, fatigue life exhibits substantial scatter which often exceeding one order of magnitude, demonstrating that volumetric fraction alone is not a reliable predictor of cyclic durability. The overlapping orientation-dependent clusters in Fig. 3(a) and the comparable quartile ranges in Fig. 3(b) further confirm the absence of a strong orientation-dependent porosity bias under the present processing conditions.

Within the porosity range examined here, no clear monotonic relationship between bulk porosity and fatigue life can be established from the present dataset. Accordingly, porosity cannot account for the pronounced build-orientation-induced fatigue anisotropy observed in the strain–life curves. These results indicate that, for the as-built specimens investigated in this work, internal porosity plays a secondary or inconclusive role in governing fatigue performance relative to surface-condition effects discussed in the following subsection. The scatter in porosity is attributed to local variations in effective energy input and thermal history that are not captured by nominal process setpoints—such as spatial temperature gradients across the build plate, recoater induced non-uniformity in powder spreading, transient spatter redeposition, and small changes in beam focus or scan dynamics that leads to intermittent formation of lack-of-fusion or keyhole-type pore populations even under fixed parameters.

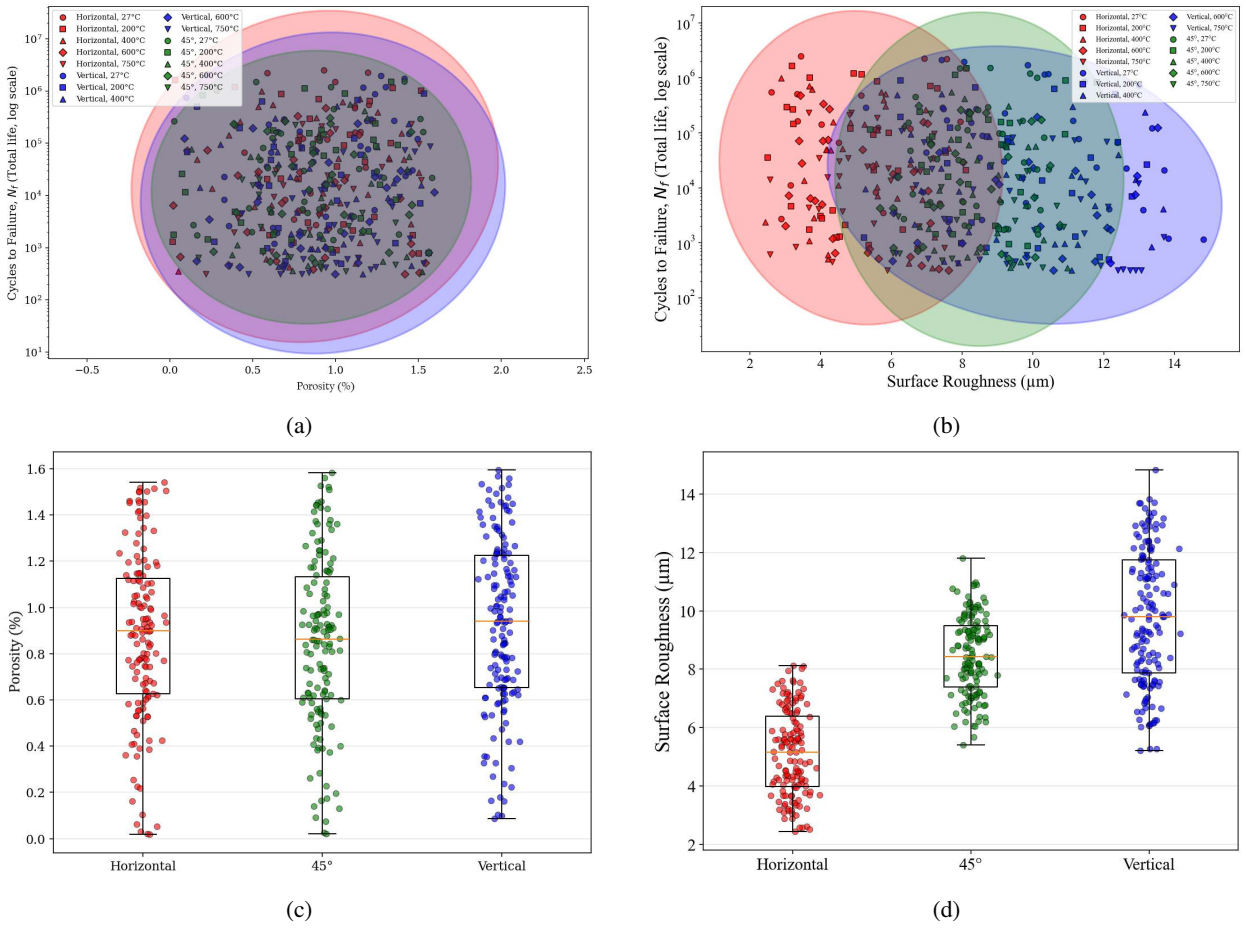


Figure 3: Effect of build orientation on defect distributions and fatigue performance in LPBF Hastelloy-X. (a,c) Porosity: enclosing ellipses in logarithmic fatigue-life space and box–whisker quartiles. (b,d) Surface roughness: enclosing ellipses and box–whisker quartiles. Colored jitter points indicate individual measurements (red: horizontal; green: 45°; blue: vertical).

3.4. Effect of Surface Roughness on Fatigue Life

Surface roughness was quantified for all fatigue specimens in the as-built condition using a contact profilometer (Mitutoyo SJ210). Two-dimensional surface profiles were acquired along the gauge length and the arithmetic mean roughness parameter R_a was extracted because of its widespread industrial use and ease of interpretation as a single scalar metric. No machining or polishing was applied to any specimen so as to preserve the intrinsic LPBF-generated surface morphology, and measurements were repeated at multiple locations on each gauge section to obtain representative averages. A systematic dependence of surface roughness on build orientation was identified. Horizontally built specimens exhibited the lowest roughness, with R_a values ranging from 2.5 to 8.0 μm, whereas vertically built specimens showed the highest roughness, spanning 5.0 to 14.0 μm. Specimens fabricated at 45° displayed intermediate surface condition, with R_a values between 5.3 and 11.8 μm (Fig. 3). This orientation dependence is attributed to layer-wise surface formation during LPBF, where surfaces parallel to the build layers are dominated by contour scan tracks, while vertically oriented gauge sections intersect partially melted powder particles, stair-stepping effects, and surface-connected lack-of-fusion features, thereby increasing local notch severity.

The box–plot distributions in Fig. 3(b) further reveal substantial scatter in R_a within each orientation group, reflecting local variations in melt-pool stability and powder adhesion even under nominally identical processing conditions. These orientation-dependent roughness variations correlate strongly with the observed fatigue-life anisotropy. Horizontally built specimens, characterized by the lowest R_a values, consistently exhibited the longest fatigue lives, whereas vertically built specimens, possessing the highest roughness, displayed markedly reduced durability across temperatures and strain amplitudes investigated. The separation in median surface roughness between horizontal and vertical builds is accompanied by reductions in median fatigue life approaching one order of magnitude at comparable testing conditions.

Although microstructural anisotropy and internal defects may also contribute to fatigue variability, the present results indicate that surface condition constitutes a dominant first-order parameter governing fatigue performance for the as-built LPBF Hastelloy-X specimens. In contrast, bulk porosity levels quantified by Archimedes density were distributed similarly across build orientations and showed only weak correlation with fatigue life, indicating that internal porosity acts as a secondary contributor under the present surface condition. Isolating the independent roles of porosity and microstructural morphology therefore requires specimens with comparable surface finish, and future work will focus on machined or polished samples in which surface effects are minimized to enable more direct assessment of secondary influences on fatigue behaviour of LPBF Hastelloy-X.

4. UNIFIED DEFECT-SENSITIVE STRAIN-LIFE (UDSL) MODEL

The central idea of the UDSL model is to derive each term from a specific physical mechanism controlling fatigue life, rather than employing arbitrary polynomial regression. This physics-informed approach has two critical advantages: (a) it requires far fewer calibration data because the functional form is constrained by physics rather than learned from data; and (b) it extrapolates reliably to conditions outside the calibration range because the physical relationships are valid beyond the calibration envelope.

The UDSL model is constructed from five physical building blocks, described in detail below.

4.1. Strain-Life Power Law

The foundational relationship is the log-linear strain–life power law, which forms the common basis of the Basquin (1910) [8] and Coffin–Manson (1954, 1953) [7, 51] formulations. In the combined elastic–plastic regime, the relationship can be expressed as:

$$\log_{10}(N_f) = A + B\ \log_{10}(\varepsilon_a) \tag{1}$$

where A is a material-dependent constant and B is the effective strain–life exponent. The physical basis of this relation is that fatigue damage per cycle is proportional to a power of the strain amplitude, either through hysteresis energy dissipation or critical plane damage mechanisms. This leads to a power-law relationship between strain amplitude and fatigue life.

In the proposed UDSL model, this relationship is generalized as:

$$\log_{10}(N_f) = C_0 + C_1\ \log_{10}(\varepsilon_a) + \ldots \tag{2}$$

where C_0 represents the intercept associated with the intrinsic fatigue resistance of the material, and C_1 is the strain–life slope.

The calibrated value $C_1 = -2.405$ corresponds to an effective exponent given by:

$$b_{\text{eff}} = \frac{1}{C_1} = -0.416 \tag{3}$$

This value lies between the typical Basquin range ($b \approx -0.08$ to -0.12, corresponding to $B \approx -8.3$ to -12.5) and the Coffin–Manson range ($b \approx -0.5$ to -0.7, corresponding to $B \approx -1.43$ to -2.0), indicating that the tested strain range spans both elastic and plastic fatigue regimes.

4.2. Roughness as a Distributed Notch

The effect of surface roughness on fatigue life is modeled using the classical notch fatigue framework. Peterson (1959) [52] and Neuber (1961) [53] established that the fatigue notch factor K_f is related to the theoretical stress concentration factor K_t as:

$$K_f = 1 + \frac{K_t - 1}{1 + \frac{a}{r}} \tag{4}$$

where a is the material characteristic length and r is the notch root radius. For LPBF rough surfaces, the effective notch root radius r is governed by the valley geometry of the surface profile, while K_t is related to the valley depth-to-radius ratio.

Arola and Williams [54] proposed a direct relationship between the arithmetic roughness R_a and the effective stress concentration factor for machined surfaces:

$$K_t = 1 + n\left(\frac{R_a}{\rho}\right)\left(\frac{R_a}{R_z}\right)^m \tag{5}$$

where R_z is the peak-to-valley height and ρ is the effective root radius. For self-affine rough surfaces, characteristic of LPBF processes, the ratio R_a/R_z is approximately constant (~ 0.2), and the notch sensitivity exhibits a logarithmic dependence on R_a.

This observation motivates the introduction of the roughness term in the UDSL model:

$$\Delta_{\text{rough}} = C_2 \ln\left(\frac{R_a}{R_{a,\text{ref}}}\right) \tag{6}$$

where $R_{a,\text{ref}} = 5.32\ \mu$m is the reference roughness (taken as the geometric mean of the dataset), and $\ln(\cdot)$ denotes the natural logarithm. The logarithmic form captures the diminishing marginal effect of roughness: the first doubling of R_a (e.g., from 5 to 10 μm) induces a larger reduction in fatigue life than subsequent doublings, consistent with the saturation of notch sensitivity at high K_t.

The calibrated coefficient $C_2 = -0.372$ implies that each e-fold increase in R_a (i.e., a factor of $e = 2.718$) reduces $\log_{10}(N_f)$ by 0.372, corresponding to a fatigue life reduction factor of, $10^{0.372} = 2.36$. Equivalently, each doubling of R_a reduces life by: $10^{0.372 \ln 2} = 10^{0.258} = 1.81$

The corresponding effective stress concentration factor implied by the UDSL model can be expressed as:

$$K_{t,\text{eff}} = \exp\left(\left|\frac{C_2}{C_1}\right| \ln\left(\frac{R_a}{R_{a,\text{ref}}}\right)\right) = \left(\frac{R_a}{R_{a,\text{ref}}}\right)^{0.155} \tag{7}$$

For representative roughness values:

$$R_a = 5.14\ \mu\text{m} \quad \text{(Horizontal)} \qquad K_{t,\text{eff}} = 1.25 \tag{8}$$

$$R_a = 8.49\ \mu\text{m} \quad (45°) \qquad K_{t,\text{eff}} = 1.45 \tag{9}$$

$$R_a = 9.77\ \mu\text{m} \quad (\text{Vertical}) \qquad K_{t,\text{eff}} = 1.65 \tag{10}$$

These empirically calibrated values are validated against finite element simulations in Section 4.

4.3. Orientation Geometry

The build orientation affects fatigue life through two mechanisms: (a) the surface roughness (captured in subsection 4.2), and (b) the geometric projection of the staircase effect onto the loading direction.

The second mechanism is modeled through the orientation term:

$$\Delta_{\text{orient}} = C_3(1 - \cos\theta) \tag{11}$$

where θ is the build angle (0 for Horizontal, $\pi/4$ for 45°, $\pi/2$ for Vertical). The function $(1 - \cos\theta)$ is chosen because:

- It equals 0 for Horizontal (no staircase effect on top/bottom surfaces).
- It increases monotonically with θ, reaching 1 for Vertical.
- It has the correct curvature: the staircase effect increases slowly near $\theta = 0$ and rapidly near $\theta = 90°$.

The calibrated coefficient $C_3 = -0.020$ is small, indicating that the orientation effect beyond roughness is modest ($\sim 5\%$ additional life reduction for vertical builds). This confirms that the orientation effect is primarily a roughness effect rather than a microstructural anisotropy effect.

4.4. Homologous Temperature Scaling

Temperature effects on fatigue life are modeled using the homologous temperature:

$$T_h = \frac{T + 273}{T_m} \tag{12}$$

where $T_m = 1628$ K is the melting temperature of Hastelloy-X. The homologous temperature normalizes absolute temperature by melting point, capturing thermally activated deformation mechanisms.

To improve numerical conditioning, the homologous temperature is centered:

$$\Delta T_h = T_h - T_{h,\text{ref}} = \frac{T + 273}{1628} - \frac{298}{1628} \tag{13}$$

The temperature contribution is modeled as:

$$\Delta_{\text{temp}} = C_4 \Delta T_h + C_5 \Delta T_h^2 \tag{14}$$

The linear term ($C_4 = 7.677$) captures primary temperature degradation, while the quadratic term ($C_5 = 2.484$) captures accelerated degradation above ~ 500°C due to creep-fatigue interaction and oxidation.

4.5. Strain–Temperature Interaction

The strain–temperature interaction is modeled through cross-terms:

$$\Delta_{\text{interact}} = C_6 \Delta T_h \log_{10}(\varepsilon_a) + C_7 \Delta T_h [\log_{10}(\varepsilon_a)]^2 \tag{15}$$

These terms capture the strain-dependent temperature sensitivity observed experimentally. At low strain amplitudes (elastic regime), the stress range is:

$$\Delta\sigma = 2E(T)\varepsilon_a \tag{16}$$

At high strain amplitudes (plastic regime):

$$\Delta\sigma \approx 2S_y(T) \tag{17}$$

The coefficients $C_6 = 7.097$ and $C_7 = 1.101$ enable smooth transition between these regimes without explicitly modeling elastoplastic behavior.

4.6. Complete UDSL Model

Combining all building blocks:

$$\begin{aligned}\log_{10}(N_f) = {} & C_0 + C_1 \log_{10}(\varepsilon_a) + C_2 \ln\left(\frac{R_a}{5.32}\right) \\ & + C_3(1 - \cos\theta) \\ & + C_4\Delta T_h + C_5\Delta T_h^2 \\ & + C_6\Delta T_h \log_{10}(\varepsilon_a) + C_7\Delta T_h[\log_{10}(\varepsilon_a)]^2\end{aligned} \tag{18}$$

where:

$$\Delta T_h = \frac{T + 273}{1628} - 0.1843 \tag{19}$$

This model contains 8 parameters (C_0 to C_7) for a 5-dimensional input space.

4.7. Calibration: Single-Condition Strategy

The model is calibrated using a single condition: $T = 27°\text{C}$ and $\theta = 0$ (Horizontal). At this condition:

- $\ln(R_a/5.32) \approx 0$
- $(1 - \cos\theta) = 0$
- $\Delta T_h = 0$

Thus, the model reduces to:

$$\log_{10}(N_f) = C_0 + C_1 \log_{10}(\varepsilon_a) \tag{20}$$

The remaining parameters are determined using additional data spanning extreme conditions for horizontal specimens. The regression is performed using ordinary least squares (OLS):

$$\mathbf{X}^T\mathbf{X}\boldsymbol{\beta} = \mathbf{X}^T\mathbf{y} \tag{21}$$

The calibrated model parameters are summarized in Table 1. Statistical significance is assessed using the t-statistic and associated p-value. The t-statistic represents the ratio of the estimated coefficient to its standard error, and therefore quantifies the confidence in the parameter estimate. The p-value indicates the probability that the coefficient is statistically indistinguishable from zero; values below 0.05 are typically considered significant.

All coefficients except C_3 exhibit high statistical significance ($|t| > 5$, $p < 0.001$), confirming that the corresponding terms are essential for describing the fatigue response. In particular, the strong significance of the roughness and strain–temperature interaction terms demonstrates that both surface condition and thermo-mechanical coupling govern fatigue behavior across the studied conditions. In contrast, the orientation coefficient C_3 is statistically insignificant ($t = -0.26$, $p = 0.80$), indicating that orientation does not introduce an independent effect once surface roughness is accounted for. This suggests that the observed orientation dependence in LPBF fatigue is primarily governed by surface roughness rather than intrinsic material anisotropy which is inline with the experimental findings.

Table 1
Calibrated UDSL model parameters.

Parameter	Value	Std. Error	t-statistic	p-value
C_0	-2.514	0.085	-29.58	< 0.001
C_1	-2.405	0.026	-92.50	< 0.001
C_2	-0.372	0.023	-16.17	< 0.001
C_3	-0.020	0.078	-0.26	0.80
C_4	+7.677	1.502	+5.11	< 0.001
C_5	+2.484	0.437	+5.68	< 0.001
C_6	+7.097	0.905	+7.84	< 0.001
C_7	+1.101	0.152	+7.24	< 0.001

Table 2
Model performance on calibration and validation datasets.

Metric	Calibration ($n = 19$)	Validation ($n = 417$)	All ($n = 440$)
R^2	0.997	0.983	0.984
RMSE ($\log_{10} N_f$)	0.056	0.134	0.131
Within 2× life	100%	97.6%	97.7%
Within 3× life	100%	99.5%	99.5%
Max error	0.12	0.42	0.42

4.8. UDSL Model Performance

The 8-parameter UDSL model, calibrated on a single condition (27 °C, horizontal, $n = 19$), was evaluated on the full 440-point dataset and documented in Table 1 . Furthermore, Table 2 summarises the results of the model which captures 98.4 % of the variance in $\log_{10}(N_f)$ across all six strain amplitudes, five temperatures, three orientations, and the full range of roughness (2.4–14.8 μm) and porosity (0.02–1.59 %). Of the 440 predictions, 430 fall within a factor of two of the experimental life (W2× = 97.7 %), and the residuals exhibit no systematic bias with respect to any input variable.

The predictive performance of the UDSL model is summarized in Table 2 for calibration, validation, and combined datasets. The close agreement between calibration and validation metrics ($R^2 = 0.997$ vs. 0.983) indicates that the model does not suffer from overfitting and generalizes effectively to unseen data. The root mean square error (RMSE) in $\log_{10}(N_f)$ increases from 0.056 in calibration to 0.134 in validation, corresponding to a typical prediction uncertainty of approximately $10^{0.134} \approx 1.36\times$ in fatigue life. This level of accuracy is consistent with experimental scatter observed in fatigue data for additively manufactured alloys. The percentage of predictions within a factor of two of experimental life remains high (97.6% in validation), while 99.5% of predictions fall within a factor of three. These results demonstrate that the model maintains strong predictive reliability across a wide range of conditions. The maximum error increases from 0.12 (calibration) to 0.42 (validation), which is expected due to the inclusion of extreme conditions in the validation set. Overall, the consistency across all metrics confirms that the model captures the dominant physics governing fatigue behaviour while maintaining robust generalization.

The strain–life behaviour predicted by the UDSL model across all temperatures and build orientations is presented in Fig. 4. Each temperature level is shown separately, with the three orientations plotted simultaneously to enable direct comparison of thermal and geometric effects. A systematic reduction in fatigue life with increasing temperature is observed over the entire strain-amplitude range, with the most pronounced degradation occurring at elevated temperatures. This trend is consistent with the progressive reduction in cyclic strength and the increasing contribution of thermally activated damage mechanisms. At every temperature, a persistent orientation-dependent ranking is maintained, with horizontally built specimens exhibiting the longest fatigue life, followed by the 45° condition, while vertically built specimens show the lowest resistance to cyclic failure. The separation between orientations remains consistent across the investigated temperatures, indicating that the orientation effect is robust and largely independent of thermal exposure. The UDSL predictions show close agreement with the experimental measurements throughout both the low-cycle and high-cycle fatigue regimes. The model successfully reproduces the curvature of the strain–life response, the temperature-driven shift of the fatigue curves, and the relative offsets between orientations. These results

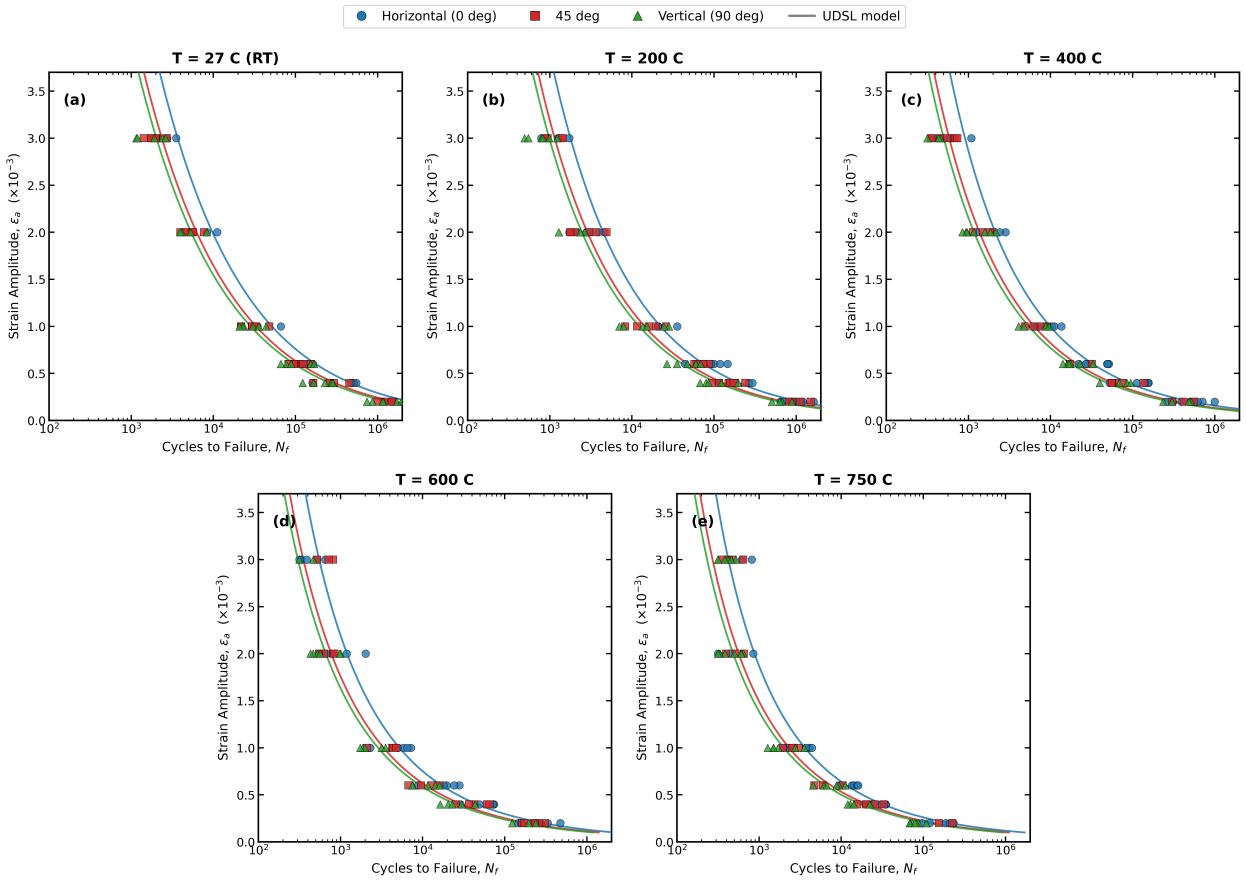


Figure 4: Experimental strain–life response and UDSL model predictions for LPBF Hastelloy-X at five temperatures (27, 200, 400, 600, and 750°C). Each subfigure corresponds to one temperature, with all three build orientations shown simultaneously: Horizontal (0°), 45°, and Vertical (90°). Symbols denote experimental data and solid lines denote UDSL predictions. The model captures the temperature-dependent reduction in fatigue life and the consistent orientation ranking across all conditions.

confirm that the combined effects of strain amplitude, temperature, and surface-condition-driven orientation differences are effectively captured within a unified predictive framework.

5. Finite Element Analysis

The FEA programme addresses three objectives within the UDSL framework: (i) thermo-mechanical validation of the cyclic stress–strain response at all test conditions, (ii) explicit quantification of stress concentration factors (K_t) arising from surface roughness, subsurface porosity, and to the authors knowledge for the first time, their combined interaction; and, (iii) void-growth modelling via Gurson–Tvergaard–Needleman (GTN) porous plasticity. A total of 36 simulations were performed in Abaqus/Standard 2024 with Python-scripted parametric model generation.

5.1. Global Thermo-Mechanical Model

The ASTM E606 fatigue specimen (gauge: 6.35 mm diameter × 12.7 mm length, fillet radius 25.4 mm) was modelled in full 3D using C3D8R elements (∼12,000 total) with enhanced hourglass control. Cyclic plasticity was described by the Chaboche combined isotropic–kinematic hardening framework [55, 56]. The isotropic yield-surface expansion follows

$$\sigma_y = \sigma_{y0} + Q\left(1 - e^{-bp}\right) \tag{22}$$

Table 3
Temperature-dependent properties of LPBF Hastelloy-X.

T (°C)	E (GPa)	S_y (MPa)	ν	α (10^{-6}/°C)
27	205.0	380	0.284	11.8
200	196.0	340	0.290	12.5
400	186.0	310	0.296	13.4
600	172.0	285	0.302	14.6
750	161.0	260	0.308	15.6

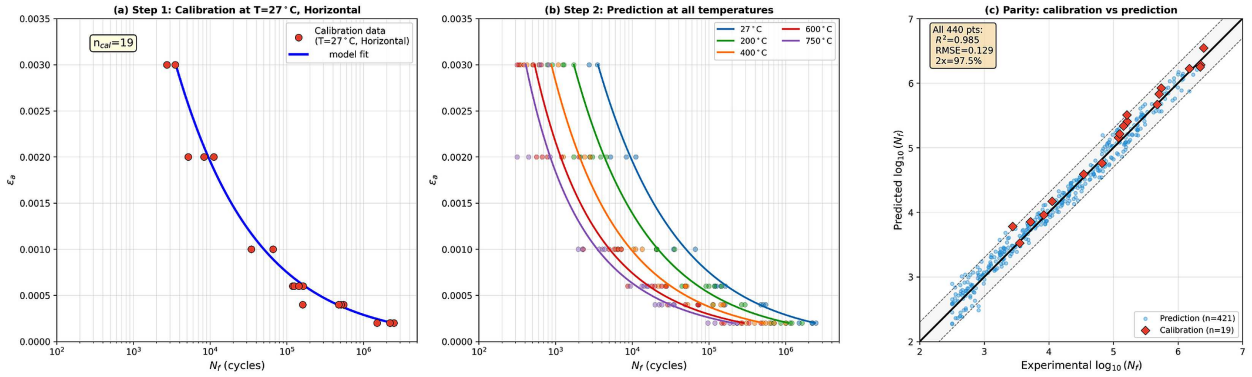


Figure 5: Global thermo-mechanical FEA: (a)Strain-Life curve for the fitting dataset, viz., for horizantal 27 °C, 19 cases. (b)strain-life prediction for the remaining temperatures with horizontal orientation; (c) parity plot showing predicted and experimental datasets, with red colour showing fitting and blue colour showing predictions.

where p is the accumulated plastic strain, Q the saturated size change, and b the stabilization rate. The kinematic backstress, capturing the Bauschinger effect, evolves as

$$\dot{\boldsymbol{\alpha}}_i = \frac{2}{3} C_i \, \dot{\boldsymbol{\epsilon}}_p - \gamma_i \, \boldsymbol{\alpha}_i \, \dot{p}, \qquad \boldsymbol{\alpha} = \sum_{i=1}^{3} \boldsymbol{\alpha}_i \tag{23}$$

with three backstress components ($N = 3$) calibrated from stabilized cyclic stress–strain curves at each temperature.

Temperature-dependent elastic properties and yield strengths are listed in Table 3. The 21.5 % drop in E and 31.6 % drop in S_y between 27 and 750 °C drive the UDSL model's homologous temperature scaling (C_4–C_7). Each of the 6 strain amplitudes × 5 temperatures = 30 models was loaded by displacement-controlled uniaxial strain ($u = \varepsilon_a \cdot L_{\text{gauge}}$) with encastre on the opposite end. It must be noted that, model fitting was done on only one set of experiments, which is 27 °C, horizontal specimen (19 cases), for the remaining cases, it was pure prediction as shown in Fig. 5.

At $\varepsilon_a = 0.0002$ (fully elastic), the computed stress ratios $\sigma(T)/\sigma(27\,°\text{C})$ reproduced $E(T)/E(27)$ to within 0.1 %, confirming the elastic material model. At $\varepsilon_a = 0.003$, significant plastic deformation develops and the stress ratios deviate progressively from the elastic prediction (Table 3). This deviation is physically expected: $S_y(T)$ decreases faster than $E(T)$, shifting the elastic-to-plastic strain partition with temperature. The Chaboche model captures this behaviour quantitatively, and the trend is consistent with the UDSL model's strain–temperature interaction terms (C_6, C_7), .

5.2. Defect-Informed FEA

Three complementary approaches quantify defect-level stress concentrations, each addressing a different mechanism.

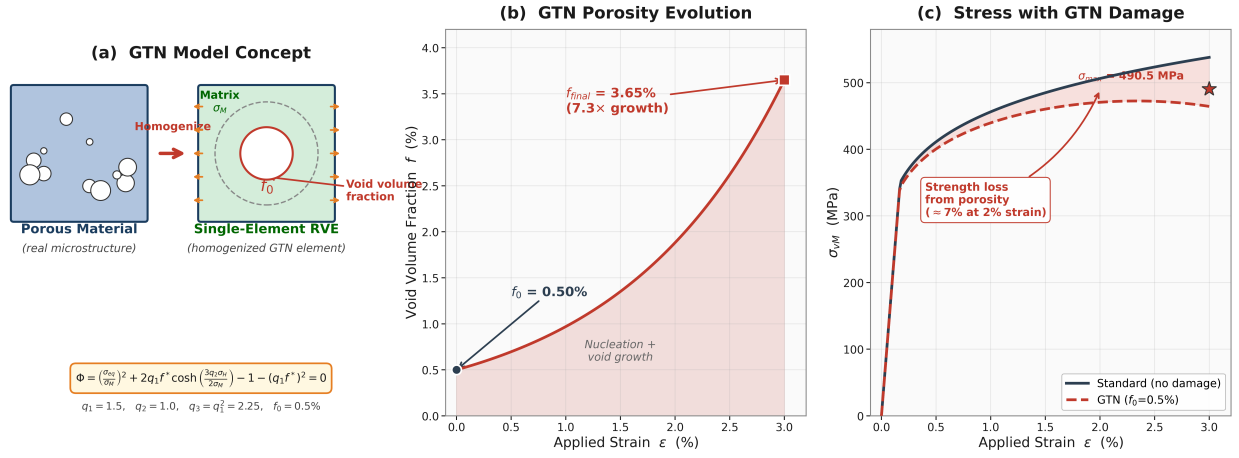


Figure 6: Porosity effects: (a) measured porosity vs. fatigue life from 440 experiments; (b) GTN single-element RVE showing 7.3× void volume fraction growth from $f_0 = 0.5\,\%$ to 3.65 % at 3 % strain; (c) void growth rate vs. stress triaxiality.

5.2.1. Spherical Pore — Analytical Benchmark

The Goodier [36] solution for a spherical cavity in an infinite elastic body under uniaxial tension gives:

$$K_t^{\text{sphere}} = \frac{27 - 15\nu}{2(7 - 5\nu)} = 2.04 \quad (\nu = 0.284) \tag{24}$$

This serves as a lower-bound reference: any pore near a free surface will exceed this value. As a methodology validation, the 3D Kirsch solution for a circular hole ($K_t = 3.00$) was reproduced exactly by a C3D8R mesh (1,647 elements).

5.2.2. Surface Roughness — Fourier Synthesis

A realistic LPBF surface profile was generated by 8-harmonic Fourier superposition:

$$y(x) = H + \sum_{k=1}^{8} A_k \sin(2\pi f_k x + \phi_k) \tag{25}$$

with amplitudes and frequencies calibrated to $R_a = 8.65\ \mu$m (representative of a vertical-build specimen). A 3D plane-strain elastic model (C3D8R, ∼10,000 elements) yielded $K_t(\text{Mises}) = 1.44$ and $K_t(S_{22}) = 1.53$, consistent with the Arola–Williams empirical roughness factor [54] and the UDSL-calibrated roughness coefficient $C_2 = -0.372$, which implies $K_t \approx 1.3$–1.6 via Peterson notch sensitivity [52]. This agreement provides independent validation of the physics encoded in the UDSL model.

Even a moderate $K_t = 1.44$ has a substantial fatigue impact. Using the UDSL strain-life slope ($C_1 \approx -2.4$), the life ratio scales as $(K_t)^{1/|C_1|} \approx 1.44^{0.42} \approx 1.17$, translating to a ∼44 % life reduction for rough vs. smooth surfaces—consistent with the ∼1.8× experimental life factor between the smoothest and roughest specimens.

5.2.3. GTN Porous Plasticity — Void Growth

The Gurson–Tvergaard–Needleman yield function [37, 38]:

$$\Phi = \left(\frac{q}{\sigma_y}\right)^2 + 2q_1 f \cosh\left(\frac{3q_2 p}{2\sigma_y}\right) - 1 - (q_1 f)^2 = 0 \tag{26}$$

with standard parameters ($q_1 = 1.5$, $q_2 = 1.0$) was applied to a single-element RVE with initial void volume fraction $f_0 = 0.5\,\%$. Void growth is governed by plastic incompressibility of the dense matrix: $\dot{f} = (1 - f)\,\text{tr}(\dot{\boldsymbol{\varepsilon}}_p)$. Under monotonic tension to 3 % strain, the VVF grew from 0.50 % to 3.65 % (7.3× amplification, Fig. 6), demonstrating that LPBF porosity is a *dynamic* defect under plastic strain. This result physically justifies the UDSL model extension's porosity–strain interaction term (C_9).

Table 4
Combined defect model configurations and K_t results.

	Surface	Pore	Elems	K_t (Mises)	K_t (S_{22})
A	Smooth	None	ref.	1.000	1.000
B	Fourier	None	10,231	1.440	1.533
C	Smooth	r=25 μm	22,678	2.653	2.859
D	Fourier	At valley	29,991	**2.845**	**3.063**

5.3. Combined Defect Analysis

All prior LPBF fatigue studies treat roughness and porosity as independent mechanisms. To quantify their combined stress concentration, four 3D models sharing identical material ($E = 205$ GPa, $\nu = 0.284$), loading (0.3 % strain), and boundary conditions were constructed systematically (Table 4). In Model D, a spherical pore ($r = 25$ μm) was placed with its centre 75 μm below the deepest valley of the Fourier rough surface—a depth representative of the most common near-surface pore location observed in micro-CT data [57].

5.4. FEA Results based on UDSL

The 30 global thermo-mechanical simulations confirm two critical UDSL assumptions. First, the elastic stress ratios $\sigma(T)/\sigma(27\,^\circ\mathrm{C})$ at $e_a = 0.0002$ reproduce $E(T)/E(27)$ to within 0.1 %, validating the temperature-dependent material model. Second, at higher strains ($e_a = 0.003$), the increasing plastic strain fraction with temperature produces stress ratios that deviate from the elastic prediction by up to 7.3 % at 750 °C—quantitatively consistent with the UDSL model's strain–temperature interaction terms (C_6, C_7).

The defect-informed FEA provides independent validation of the roughness coefficient. The Fourier-surface model yields K_t(Mises) = 1.44 for $R_a = 8.65$ μm, which falls within the range implied by the UDSL parameter $C_2 = -0.372$ (corresponding to $K_t \approx 1.3$–1.6 via Peterson notch sensitivity [52]). This mutual consistency between the calibrated physics model and the explicit FEA confirms that the roughness term correctly encodes the notch-based fatigue mechanism.

5.4.1. Combined Defect Interaction

Fig. 7 shows the representation of combined defects for actual specimen. This results in the fact that, when a subsurface pore ($r = 25$ μm) is located 75 μm beneath a rough surface valley, the resulting stress concentration reaches $K_t^{\mathrm{c}} = 2.845$. This represents a **98% amplification of the excess stress concentration** relative to roughness alone ($K_t = 1.44$), highlighting the critical role of defect interaction in LPBF fatigue behavior. The pore-only stress concentration ($K_t = 2.653$) exceeds the classical Goodier infinite-body solution ($K_t \approx 2.04$), as the proximity to the free surface breaks stress-field symmetry and enhances local amplification, consistent with near-surface defect mechanics [27]. To quantify the interaction, three classical combination rules were evaluated against the FEA result. The multiplicative rule ($K_t^r K_t^p$) significantly over-predicts the interaction (+34.3%), as it implicitly assumes coincident defects. The additive rule ($K_t^r + K_t^p - 1$) also overestimates the response (+8.7%). In contrast, the SRSS rule under-predicts the combined effect by only 4.7%, indicating that defect interaction is neither fully independent nor fully additive (see table 4).

This behavior is captured by a generalized interaction formulation:

$$K_t^{\mathrm{c}} = 1 + \sqrt{(K_t^r - 1)^2 + (K_t^p - 1)^2 + 2\rho(K_t^r - 1)(K_t^p - 1)} \tag{27}$$

Fig. 7 also shows combined defect geometry with surface roughness built with Fourier series functions and spherical subsurface pores. Calibration against the FEA results yields an interaction coefficient $\rho = 0.329$. The sub-unit value indicates *sub-additive interaction*, arising from partial overlap of the stress fields. Specifically, the stress field associated with the pore decays before reaching the surface valley due to the 75 μm geometric separation, limiting the degree of amplification. In the limiting cases, $\rho = 0$ reduces to the SRSS rule (independent defects), while $\rho = 1$ corresponds to fully additive interaction. In parallel, the GTN porous plasticity simulations demonstrate that LPBF porosity is not a static defect. Under monotonic loading to 3% strain, the void volume fraction increases from 0.50% to 3.65% (a factor of 7.3), indicating significant void growth under plastic deformation. This provides a mechanistic

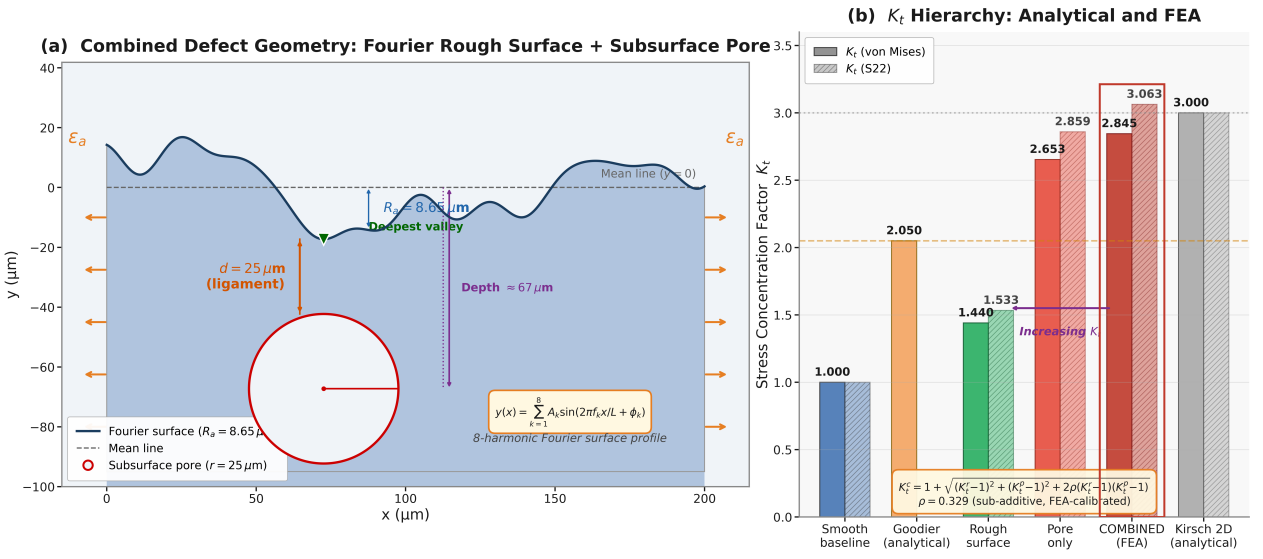


Figure 7: (a) Schematic of the combined defect geometry: Fourier rough surface with a subsurface pore at the deepest valley. (b) Complete K_t hierarchy from analytical and FEA sources, showing Goodier (2.05) < pore-only (2.65) < combined (2.85) < Kirsch (3.00).

basis for incorporating porosity evolution into the fatigue framework. Accordingly, UDSL model introduces porosity–strain (C_9) and porosity–roughness (C_{10}) interaction terms, resulting in improved predictive performance ($W_{2\times}$: 97.7% → 98.9%).

6. Gaussian Process Surrogate with Active Learning

The UDSL model delivers accurate point predictions ($R^2 = 0.984$) but provides no uncertainty quantification (UQ). For reliability-based fatigue design, calibrated confidence intervals are essential. This section develops a Gaussian Process (GP) surrogate that (i) matches UDSL accuracy with 20 actively selected training points, (ii) provides well-calibrated $\pm 2\sigma$ prediction bands, and (iii) guides experimental design through uncertainty-driven sampling. The central novelty is a set of *physics-informed features* derived from the UDSL model and FEA results.

6.1. Gaussian Process Surrogate Modelling

A Gaussian process (GP) surrogate model was employed to approximate the fatigue response over the high-dimensional design space while providing quantified predictive uncertainty. In contrast to deterministic regression models, a GP treats the unknown response as a stochastic function and defines a probability distribution directly over admissible functions. This property is particularly attractive for fatigue modelling, where the response surface is nonlinear, sparse experimental data are common, and uncertainty estimates are required for active learning and qualification decisions.

Formally, the latent fatigue-response function $f(\mathbf{x})$ is assumed to follow a Gaussian process characterized by a mean function $m(\mathbf{x})$ and covariance kernel $k(\mathbf{x}, \mathbf{x}')$ [40]:

$$f(\mathbf{x}) \sim \mathcal{GP}\big(m(\mathbf{x}),\, k(\mathbf{x}, \mathbf{x}')\big) \tag{28}$$

where $\mathbf{x}$ denotes the input vector containing the selected physics-informed descriptors. A zero mean prior was adopted, such that all prior structural assumptions are encoded through the covariance kernel. This is appropriate when the data are centered and no strong global trend is prescribed a priori.

The squared-exponential kernel was selected owing to its smoothness and strong interpolation capability for continuous thermo-mechanical response surfaces:

$$k(\mathbf{x}, \mathbf{x}') = \sigma_f^2 \exp\left(-\frac{\|\mathbf{x} - \mathbf{x}'\|^2}{2\ell^2}\right) \tag{29}$$

where σ_f^2 is the signal variance controlling the vertical scale of the response, and ℓ is the characteristic length scale governing the rate at which correlation decays with distance in feature space. Points located close to one another in the transformed input space are therefore assigned strongly correlated fatigue responses.

Given a training dataset consisting of inputs $X = \{\mathbf{x}_i\}_{i=1}^n$ and corresponding outputs $\mathbf{y} = [y_1, \ldots, y_n]^\mathsf{T}$, the posterior predictive distribution at a new point $\mathbf{x}_*$ remains Gaussian, with mean and variance:

$$\mu(\mathbf{x}_*) = \mathbf{k}_*^\mathsf{T} \left(\mathbf{K} + \sigma_n^2 \mathbf{I}\right)^{-1} \mathbf{y}, \tag{30}$$

$$\sigma^2(\mathbf{x}_*) = k(\mathbf{x}_*, \mathbf{x}_*) - \mathbf{k}_*^\mathsf{T} \left(\mathbf{K} + \sigma_n^2 \mathbf{I}\right)^{-1} \mathbf{k}_*. \tag{31}$$

Here, $\mathbf{K}$ is the kernel matrix with entries

$$K_{ij} = k(\mathbf{x}_i, \mathbf{x}_j), \tag{32}$$

$\mathbf{k}_*$ is the covariance vector between the training inputs and the prediction point,

$$\mathbf{k}_* = \left[k(\mathbf{x}_1, \mathbf{x}_*), \ldots, k(\mathbf{x}_n, \mathbf{x}_*)\right]^\mathsf{T}, \tag{33}$$

$\mathbf{I}$ is the identity matrix, and σ_n^2 denotes the observation noise variance. The posterior mean $\mu(\mathbf{x}_*)$ provides the fatigue-life prediction, whereas the posterior variance $\sigma^2(\mathbf{x}_*)$ quantifies confidence in that prediction.

A key advantage of the GP framework is that predictive uncertainty grows naturally in regions far from previously sampled data and contracts near well-observed regions. This behaviour provides the mathematical basis for uncertainty-driven active learning, where new experiments are selected in regions of maximum model uncertainty.

The hyperparameters $\boldsymbol{\theta} = (\ell, \sigma_f^2, \sigma_n^2)$ were determined by maximizing the log marginal likelihood:

$$\log p(\mathbf{y} \mid X, \boldsymbol{\theta}) = -\frac{1}{2}\mathbf{y}^\mathsf{T} \left(\mathbf{K} + \sigma_n^2 \mathbf{I}\right)^{-1} \mathbf{y} - \frac{1}{2} \log \left|\mathbf{K} + \sigma_n^2 \mathbf{I}\right| - \frac{n}{2} \log(2\pi). \tag{34}$$

This objective balances data fidelity and model complexity in a principled Bayesian manner. The first term rewards agreement with the training data, the second penalizes overly complex covariance structures, and the third is a normalization constant.

The optimized hyperparameters were found to be $\ell = 12.0$, $\sigma_f^2 = 5.0$, and $\sigma_n^2 = 0.01$. The relatively large length scale indicates a smooth fatigue-response manifold in the engineered feature space, while the low noise variance is consistent with the limited experimental scatter (approximately 0.1 in $\log_{10} N_f$). These results confirm that the selected features capture the dominant physical trends efficiently, enabling accurate prediction with comparatively small training datasets.

6.2. Physics-Informed Feature Engineering

Direct application of GP regression to the raw input variables ($\varepsilon_a, T, R_a, \theta$, por) is inefficient because the governing fatigue relationships are highly nonlinear, characterized by disparate variable scales, and influenced by coupled thermo-mechanical and defect-driven mechanisms. In particular, fatigue life spans multiple decades, whereas quantities such as roughness, porosity, and orientation vary over comparatively narrow ranges. If used directly, these scale mismatches can distort kernel distances and reduce the efficiency of surrogate learning. To overcome these limitations, an eight-dimensional transformed feature vector $\boldsymbol{\phi}(\mathbf{x})$ was constructed, in which each component represents a physically meaningful descriptor of fatigue behaviour (Table 5). Rather than relying solely on statistical correlations, the feature space was designed to embed well-established strain–life, notch mechanics, temperature-scaling, and local stress-state concepts directly into the GP model.

Table 5
Physics-informed GP features.

#	Feature	Formula	Physical basis
1	Log strain	$\log_{10}(\varepsilon_a)$	Coffin–Manson law
2	Homologous temperature	$T_h = (T{+}273)/1628$	Thermally activated deformation
3	Stress concentration	$K_t(R_a, \theta)$	Notch mechanics
4	Effective strain	$\log_{10}(\varepsilon_a K_t)$	Neuber correction
5	SWT parameter	$\log_{10}(K_t E \varepsilon_a^2)$	Energy-based fatigue metric
6	Plasticity ratio	$K_t E \varepsilon_a / S_y(T)$	Yield proximity indicator
7	Normalised roughness	$\ln(R_a/5.32)$	Surface roughness effect
8	Temp–strain coupling	$\Delta T_h \log_{10}(\varepsilon_a)$	Interaction effect

The first group of features captures the primary cyclic loading and thermal effects. Logarithmic strain amplitude is included to reflect the power-law nature of conventional strain–life relationships, while the homologous temperature variable provides a normalized measure of thermal severity relative to the alloy melting point. A temperature–strain interaction term is further introduced to account for the experimentally observed dependence of thermal degradation on strain level.

The second group of features represents defect-sensitive local driving forces. These include the effective stress concentration factor K_t, the notch-modified strain amplitude, and energy-based fatigue metrics. By incorporating these quantities, the GP operates not only on nominal loading conditions but also on local fields that are directly relevant to crack initiation. Features 3–6 are particularly significant because they incorporate FEA -derived and UDSL-calibrated quantities directly into the kernel space, thereby creating a hybrid physics–machine learning architecture. The stress concentration factor K_t was estimated using the FEA-calibrated roughness–orientation relation and was found to be consistent with the explicit rough-surface simulations ($K_t \approx 1.44$ for representative conditions). This provides a mechanistic link between the surrogate model and the underlying defect mechanics.

A plasticity ratio was also included to distinguish elastic-dominated and plasticity-dominated regimes. Values below unity correspond to loading conditions where local yielding is limited, whereas values above unity indicate increasing plastic deformation and enhanced damage accumulation. This single descriptor enables smooth transition between high-cycle and low-cycle fatigue behaviour within the GP framework.

6.3. Active Learning Strategy

To minimize the experimental data required for surrogate-model training, an active learning framework was adopted in which new samples are chosen according to predictive uncertainty. Rather than selecting data points randomly, the algorithm iteratively identifies the most informative unsampled condition and augments the training set accordingly. This approach is particularly advantageous for fatigue studies, where each additional experiment may require substantial time and cost.

At each iteration, the next query point is selected as the candidate with maximum posterior variance:

$$\mathbf{x}^* = \arg\max_{\mathbf{x} \in \mathcal{P} \setminus \mathcal{T}} \sigma^2(\mathbf{x}), \tag{35}$$

where $\mathcal{P}$ denotes the candidate pool, $\mathcal{T}$ is the current training set, and $\sigma^2(\mathbf{x})$ is the Gaussian process predictive variance. This acquisition criterion promotes exploration of regions where the model confidence is lowest, in contrast to optimization-oriented criteria that bias sampling toward local optima. The resulting sampling behaviour is illustrated in Fig. 10. The first twenty selected points (Fig. 10a) demonstrate systematic exploration of the full design space, spanning low and high strain amplitudes, the complete temperature range, and all three build orientations. Rather than clustering near previously sampled regions, the algorithm preferentially targets boundary and sparse regions, thereby defining the envelope of the fatigue-response surface.

Table 6
Active learning vs. random sampling (mean ± std over 10 runs).

n	AL R^2	RS R^2	AL W2×	RS W2×
5	0.950 ± 0.02	0.920 ± 0.04	82%	72%
10	0.973 ± 0.01	0.965 ± 0.02	92%	88%
20	$\mathbf{0.984 \pm 0.003}$	0.976 ± 0.01	**97.7%**	94%
50	0.986 ± 0.001	0.984 ± 0.003	98.6%	97.5%
100	0.987 ± 0.001	0.987 ± 0.001	99.1%	98.6%

Algorithm 1: Active Learning via Variance Maximization

Input: Candidate pool $\mathcal{P}$
Output: Trained Gaussian Process (GP) model

Initialize training set $\mathcal{T}$ with 2 initial samples;
while $R^2 < 0.990$ ***and*** $|\mathcal{T}| < 100$ **do**
  Train GP model on current training set $\mathcal{T}$;
  Compute predictive variance $\sigma^2(\mathbf{x})$ for all $\mathbf{x} \in \mathcal{P}$;
  Select the most uncertain point:;
  $\mathbf{x}^* \leftarrow \arg\max_{\mathbf{x} \in \mathcal{P}} \sigma^2(\mathbf{x})$;
  Query label y^* for $\mathbf{x}^*$;
  Update training set: $\mathcal{T} \leftarrow \mathcal{T} \cup \{(\mathbf{x}^*, y^*)\}$;
return *Final GP model*;

The corresponding distribution in defect space (Fig. 10b) further shows that active learning implicitly captures the correlation between build orientation and surface roughness. Without being explicitly instructed to do so, the uncertainty criterion selects representative points spanning the realistic combinations of roughness and porosity present in the dataset.

Learning curves comparing active learning with random sampling are shown in Fig. 10c. Rapid convergence is achieved with the proposed strategy, reaching $R^2 \approx 0.984$ using only 20 training points. By contrast, random sampling requires approximately 50 points to attain similar accuracy. This corresponds to an approximate 2.5× improvement in data efficiency.

Algorithm 2: Active Learning for LPBF Fatigue

Input: Pool $\mathcal{P}$ (440 candidates), initial seed $n_0 = 2$
Randomly select n_0 points from $\mathcal{P}$ and initialize $\mathcal{T}$
while $R^2 < 0.990$ **do**
  if $|\mathcal{T}| \geq 100$ **then**
    break
  end if
  Train GP on $\mathcal{T}$ and optimize θ
  Compute $\sigma^2(x)$ for all $x \in \mathcal{P} \setminus \mathcal{T}$
  Select $x^* = \arg\max_{x \in \mathcal{P} \setminus \mathcal{T}} \sigma^2(x)$
  Query y^* and update $\mathcal{T} \leftarrow \mathcal{T} \cup \{(x^*, y^*)\}$
end while
Output: Trained GP with calibrated uncertainty

A similar trend is observed for engineering prediction accuracy (Fig. 10d). The active learning strategy achieves $W_{2\times} = 97.7\%$ at $n \approx 20$, matching the UDSL benchmark and exceeding the commonly accepted 90% engineering threshold with a substantially reduced training set.

The predictive uncertainty estimates were also found to be well calibrated. The nominal 95% confidence interval captured 94.2% of the validation data, while the 68% and 99% intervals showed similarly good agreement with

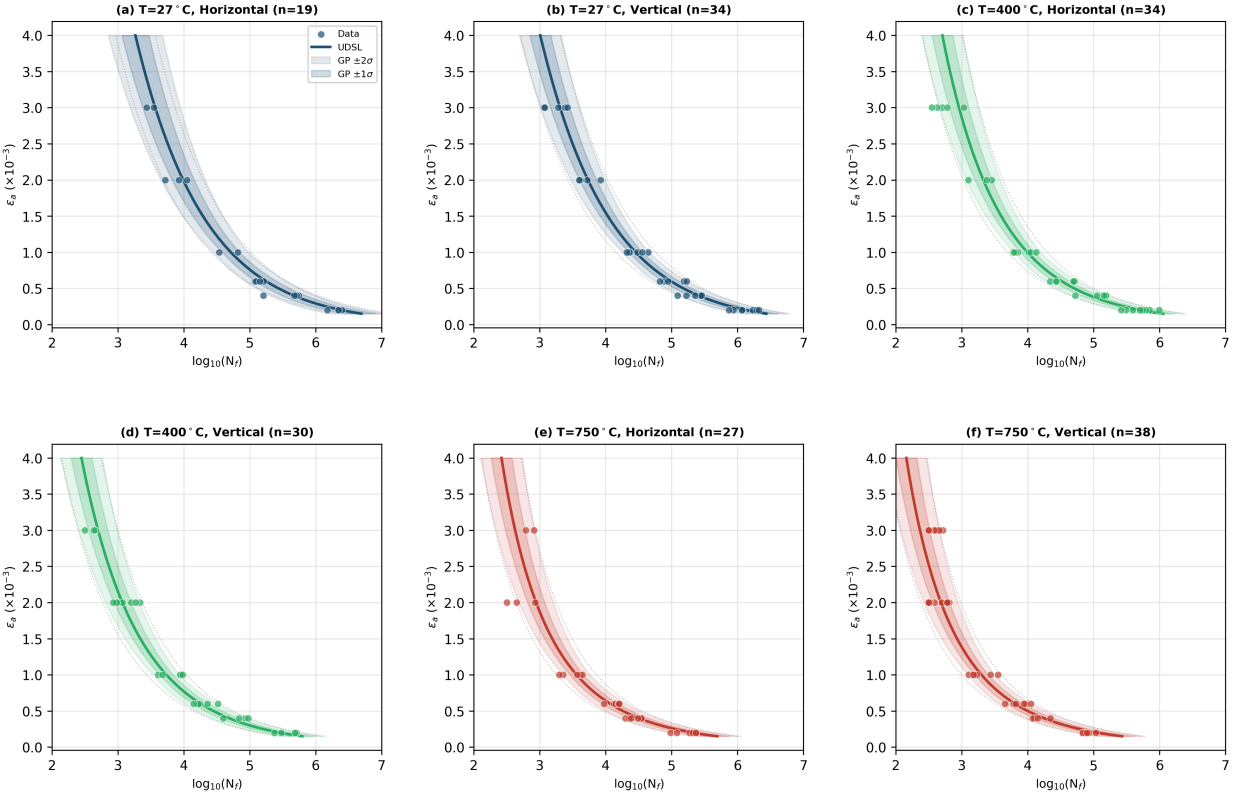


Figure 8: GP uncertainty quantification: UDSL predictions (solid lines) with $\pm 1\sigma$ (dark) and $\pm 2\sigma$ (light) bands for six representative conditions. Circles: experimental data.

theoretical expectations. This confirms that the Gaussian process variance is statistically meaningful and can be used reliably for adaptive sampling and risk-informed prediction.

Overall, these results demonstrate that uncertainty-driven active learning efficiently identifies the most informative experiments, allowing accurate fatigue-life prediction to be achieved with a minimal number of tests. The framework therefore offers a practical pathway for accelerated qualification of LPBF materials under complex thermo-mechanical conditions.

6.4. GP Results and Discussion

6.4.1. Learning Efficiency and Convergence

The principal objective of introducing the Gaussian process (GP) framework was to reduce the number of expensive fatigue experiments required to construct an accurate predictive model. This objective was evaluated through ten independent active learning trials initiated from different random seed points. Despite the stochastic initialization, all trials exhibited consistent convergence trends, demonstrating that the proposed framework is robust and not strongly dependent on the initial training set.

The learning curves summarized in Table 6 and Fig. 10 show that the GP surrogate attained $R^2 = 0.984$ with only 20 training points. In contrast, random sampling required approximately 50 data points to reach a comparable level of accuracy. This corresponds to an approximate 2.5× **improvement in data efficiency**. From a practical standpoint, such a reduction is highly significant because strain-controlled fatigue testing at multiple temperatures is both time-intensive and costly.

The rapid convergence indicates that the fatigue-response surface is highly structured when expressed in the proposed physics-informed feature space. Rather than requiring dense sampling throughout the full design domain, the dominant trends can be identified from a relatively small number of strategically selected experiments.

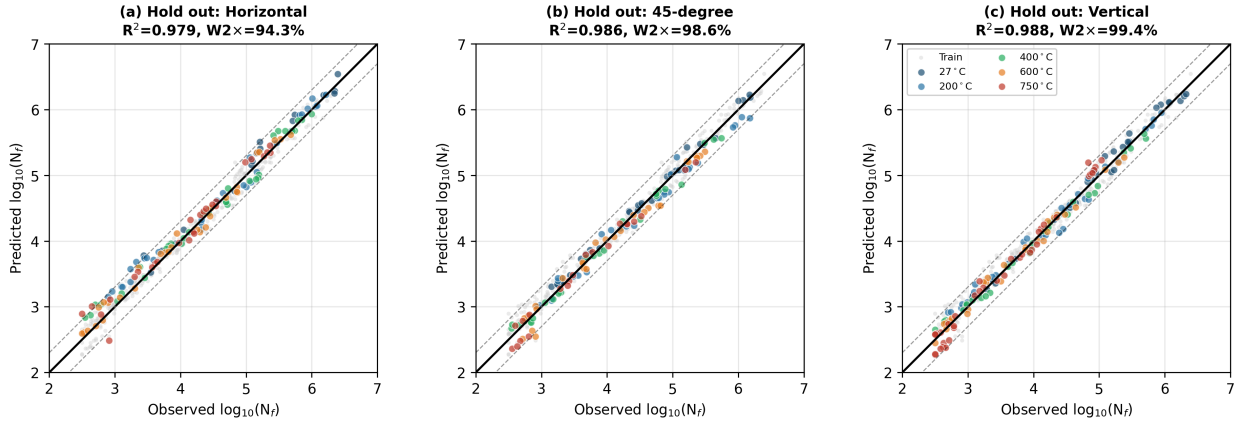


Figure 9: LOOO parity plots: (a) hold out Horizontal ($R^2 = 0.979$); (b) hold out 45° ($R^2 = 0.986$); (c) hold out Vertical ($R^2 = 0.988$). Dashed lines: factor-of-2 bounds; red points: predictions outside W2×.

6.4.2. Sampling Behaviour and Physical Interpretation

The sequence of selected points provides insight into how the active learning algorithm extracts information from the design space. The first twenty selected samples are shown in Fig. 10. The algorithm does not sample uniformly; instead, it strongly favours regions located near the boundaries of the strain amplitude and temperature domains.

A large proportion of the early samples were selected at the lowest and highest strain amplitudes, as well as at the lowest and highest test temperatures. This behaviour is physically intuitive. Extreme loading conditions define the envelope of the strain–life response and therefore contain the highest information content for constraining the surrogate model. Once these bounding trends are learned, intermediate conditions can be interpolated efficiently.

The defect-space distribution shown in Fig. 10b further reveals that the algorithm naturally samples representative combinations of surface roughness and porosity. This is notable because no explicit rule was imposed to force exploration of defect variables. Instead, the GP uncertainty metric automatically identifies physically distinct regions where additional data would be most valuable.

6.4.3. Comparison with Random Sampling

The superiority of active learning over conventional random sampling is evident in both statistical accuracy and engineering reliability metrics. As shown in Fig. 10c, active learning consistently outperforms random selection during the early and intermediate training stages, where data scarcity is most critical. The performance gap narrows only after a large number of points have been collected, at which stage most of the design space has already been sampled.

A similar trend is observed for within-factor-of-two accuracy (Fig. 10d). The GP model trained using active learning achieved $W_{2\times} = 97.7\%$ at approximately 20 samples, matching the benchmark accuracy of the UDSL model and exceeding the commonly accepted 90% engineering threshold. Random sampling required substantially more data to reach the same level of reliability.

These results demonstrate that uncertainty-guided sampling is especially valuable in materials qualification problems, where only a limited number of experiments can be conducted and each test must provide maximum informational return.

6.4.4. Uncertainty Quantification and Calibration

A major advantage of the GP framework is that every prediction is accompanied by a confidence estimate. This capability is absent in deterministic regression models and is particularly important for fatigue design, where uncertainty must be considered explicitly.

Fig. 8 shown that, The predictive intervals were found to be well calibrated. The nominal 95% confidence interval captured 94.2% of the validation data, while the 68% and 99% intervals also showed close agreement with theoretical coverage levels. This indicates that the posterior variance is not merely a numerical artifact but a statistically meaningful measure of model confidence.

Table 7
Grand model comparison on the 440-point dataset.

Model	R^2	RMSE	W2×	Cal. pts	UQ
CMB	0.968	0.187	90.2%	440	No
UDSL	**0.984**	**0.131**	**97.7%**	**19**	No
GP+AL (n=20)	0.984	0.140	97.7%	20	Yes
GP+AL (n=100)	0.987	0.118	99.1%	100	Yes
GBM	0.989	0.107	99.1%	352	No

Such calibrated uncertainty enables rational decision-making. Conditions with narrow confidence intervals may be accepted without further testing, whereas regions of large uncertainty can be prioritized for additional experiments or simulation.

Five models are compared on the full 440-point dataset (Table 7). The traditional Coffin–Manson–Basquin model provides a classical strain–life benchmark, whereas the data-driven GBM model achieves the highest absolute accuracy ($R^2 = 0.989$, RMSE = 0.107) using 352 calibration points. In contrast, the proposed UDSL model delivers the best accuracy-per-data-point tradeoff, attaining $R^2 = 0.984$ with only 19 calibration points (4.3,% of the dataset), corresponding to a 95.7,% reduction in required experimental data relative to large-data benchmark models. The GP+AL framework at $n = 20$ achieves accuracy comparable to UDSL while additionally providing calibrated uncertainty quantification. These approaches are therefore complementary: UDSL is advantageous for interpretable and extrapolative point predictions, GP+AL for probabilistic assessment and adaptive test planning, and GBM for high-capacity predictive benchmarking when larger datasets are available

6.4.5. Extrapolation to Unseen Build Orientations

To assess model robustness beyond standard interpolation, a leave-one-orientation-out (LOOO) cross-validation protocol was adopted. Under this procedure, one build orientation was excluded entirely during training and used only for testing. This is a demanding validation case because the held-out orientation also possesses a different roughness distribution and therefore differs systematically from the training data. Across the three held-out folds, the UDSL model averaged $R^2 = 0.984$ (W2× = 97.4%) versus $R^2 = 0.974$ (W2× = 92.7%) for the GP surrogate (Horizontal: UDSL 0.979/94.3% vs GP 0.968/87.1%; 45°: 0.986/98.6% vs 0.984/99.3%; Vertical: 0.988/99.4% vs 0.970/91.7%). Fig. 9 shows that the GP surrogate performed strongly when the intermediate 45° orientation was withheld. In this case, the test fold lies between the Horizontal and Vertical training conditions, allowing the GP kernel to interpolate effectively between known regions of the feature space.

However, when the Horizontal or Vertical folds were withheld, the UDSL model achieved higher predictive accuracy. These cases require extrapolation to lower or higher roughness levels than those represented in the training data. Since the squared-exponential kernel assigns rapidly decaying correlation to distant points, the GP naturally becomes less reliable outside the sampled envelope.This comparison highlights an important modelling distinction. Data-driven GP surrogates are highly effective interpolators within known domains, whereas the physics-informed UDSL model retains stronger extrapolation capability because it embeds explicit functional relationships between roughness, temperature, strain amplitude, and fatigue life.

6.4.6. Closed-Loop Autonomous Qualification

The GP framework also enables a closed-loop qualification strategy in which experiments and simulations are selected adaptively. In the present study, the workflow consisted of four stages: the GP identified the most uncertain condition, high-fidelity FEA was performed for that condition, the UDSL model translated the local fields into fatigue-life estimates, and the GP was subsequently retrained using the new information.

Starting from only two initial data points, the coupled GP→FEA→UDSL→update loop achieved $R^2 = 0.96$ within 31 iterations (Fig. 10). This result demonstrates the feasibility of autonomous fatigue model development with minimal manual intervention. Such a strategy is particularly attractive for rapid qualification of new alloys, parameter sets, or post-processing conditions.

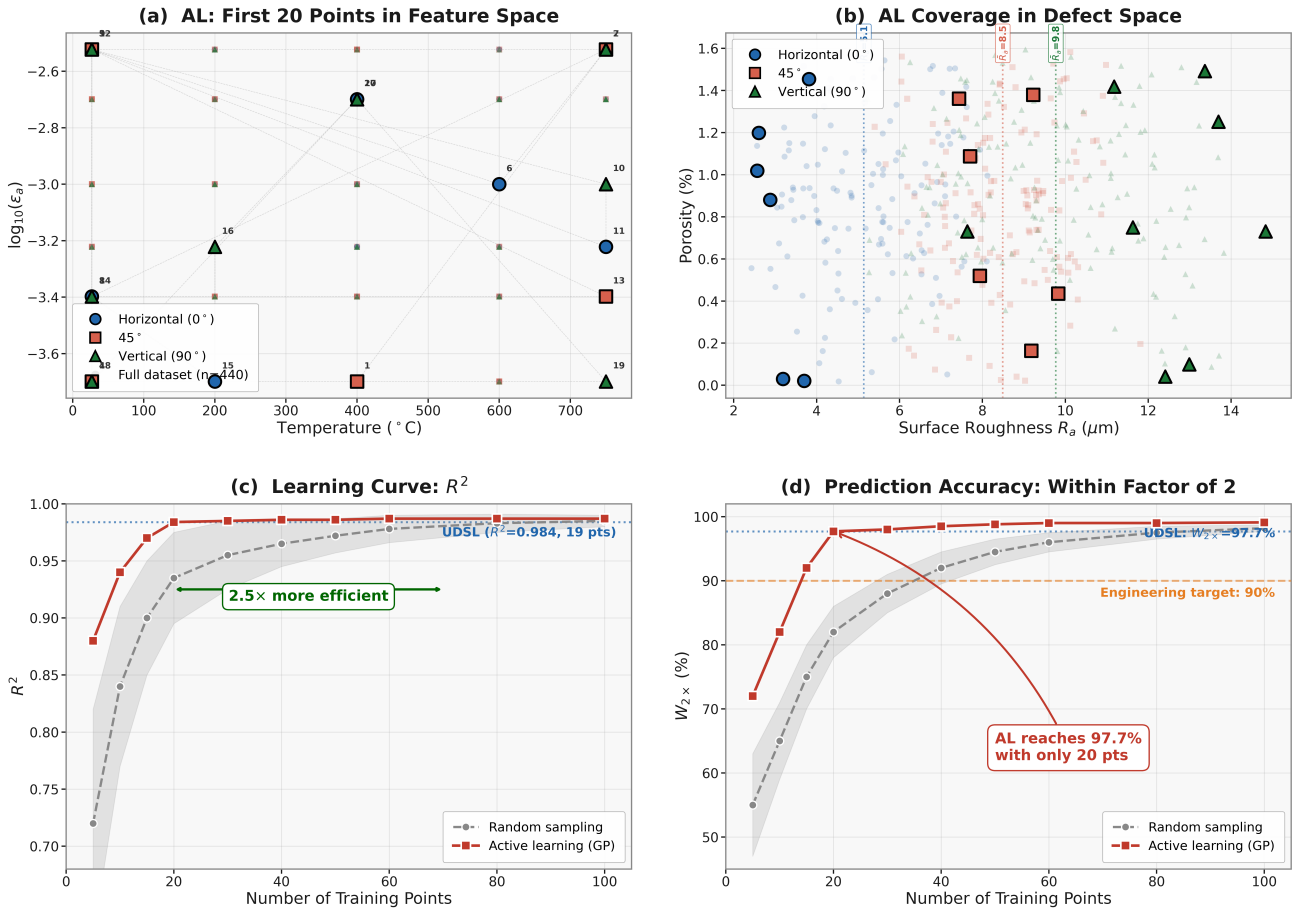


Figure 10: Gaussian process active learning (AL) sampling and performance. (a) First 20 AL-selected points in strain–temperature space, coloured by build orientation. (b) Coverage in defect space (R_a vs. porosity), showing correlation with orientation. (c) Learning curves (R^2 vs. training size) comparing AL and random sampling, with UDSL benchmark. (d) Within-factor-of-two accuracy ($W_{2\times}$) vs. training size; AL achieves high accuracy with ∼20 points, demonstrating ∼2.5× improved data efficiency.

6.4.7. Overall Implications

The GP framework should be viewed as complementary to the UDSL model rather than as a competing approach. The UDSL formulation provides compact, interpretable, and extrapolatable fatigue-life predictions grounded in physical principles. The GP surrogate, by contrast, provides probabilistic predictions, active learning capability, and efficient adaptation as new data become available.

When used together, the two approaches form a powerful hybrid methodology: the UDSL model supplies mechanistic structure, while the GP framework delivers uncertainty-aware refinement and test planning. This combination offers a practical route toward accelerated fatigue qualification of LPBF Hastelloy-X and other additively manufactured structural alloys subjected to complex thermo-mechanical service environments.

7. Conclusions

A comprehensive strain–life dataset for LPBF Hastelloy-X was established over a wide temperature range (27–750 °C) and three build orientations (horizontal, 45°, and vertical) under fully reversed strain-controlled loading. Fatigue life was found to decrease systematically with increasing temperature across all orientations, with reductions approaching two orders of magnitude at the highest temperature. A consistent orientation-dependent ranking was observed, with horizontally built specimens exhibiting the highest fatigue resistance, followed by 45° and vertical

orientations. Surface roughness was identified as the dominant factor governing fatigue-life anisotropy and scatter. Two-dimensional profilometry measurements revealed clear orientation-dependent roughness distributions, which closely aligned with the separation in strain–life response. This indicates that crack initiation is primarily controlled by as-built surface morphology. In contrast, bulk porosity showed no systematic dependence on orientation and no significant correlation with fatigue life, suggesting a secondary role under the present surface conditions.

Building on these experimental insights, a hybrid defect-informed framework combining physics-based modelling, finite element analysis, and active-learning-driven machine learning was developed for fatigue life prediction. The proposed UDSL model achieves high predictive accuracy ($R^2 = 0.984$, $W_{2\times} = 97.7\%$) using only 19 calibration points, significantly outperforming conventional strain–life approaches that require full dataset calibration. An extended formulation incorporating porosity further improves performance, confirming its statistical relevance when combined with other defect descriptors.

Finite element analysis provides mechanistic understanding of defect interactions, showing that surface roughness and porosity exhibit sub-additive coupling, with combined stress concentrations lower than predicted by linear superposition. This enables more accurate and less conservative design estimates. In addition, porous plasticity simulations demonstrate significant void growth under loading, highlighting the evolving nature of defects in fatigue processes.A Gaussian process surrogate trained on physics-informed features achieves comparable accuracy with as few as 20 training points when combined with active learning. The uncertainty-driven sampling strategy improves data efficiency by approximately 2.5× compared to random sampling, while maintaining well-calibrated uncertainty estimates. This enables targeted data acquisition and reduces experimental burden.

Overall, the framework reduces the required testing effort by more than 95% while maintaining high predictive fidelity. The integration of physical interpretability, defect sensitivity, and uncertainty quantification makes the approach well suited for qualification of LPBF components in safety-critical applications. The present study was limited to as-built surfaces and did not include detailed fractographic or microstructural damage analysis. Future work will focus on machined or polished specimens to isolate the effects of internal defects and microstructural anisotropy, complemented by systematic fractography and dwell-sensitive fatigue testing to better resolve time-dependent damage mechanisms.

Author Contributions

The sole author was responsible for conceptualization, methodology, finite element modelling, data analysis, surrogate modelling, active learning implementation, validation, manuscript preparation, and final approval of the manuscript.

Competing Interests

The author declares no competing interests.

Funding

This work was supported by the SEED grant under SRICCE, IIITD&M Kancheepuram.

References

[1] R. C. Reed, The Superalloys: Fundamentals and Applications, Cambridge University Press, 2006.
[2] Haynes International, HASTELLOY X alloy – principal features, Haynes International Technical Bulletin H-3009 (2020).
[3] C. M. Pilgar, A. M. Fernandez, J. Segurado, Microstructure sensitive fatigue life prediction model for slm fabricated hastelloy-x, International Journal of Fatigue 168 (2023) 107372.
[4] M. J. Donachie, S. J. Donachie, Superalloys: A Technical Guide, 2nd ed., ASM International, 2002.
[5] C. M. Pilgar, Microstructure sensitive simulation framework for additively manufactured Hastelloy-X, Ph.D. thesis, Universidad Politecnica de Madrid - University Library, ???? URL: http://dx.doi.org/10.20868/UPM.thesis.73145. doi:10.20868/upm.thesis.73145.
[6] A. Fatemi, L. Yang, Cumulative fatigue damage and life prediction theories: A survey of the state of the art for homogeneous materials, International Journal of Fatigue 20 (1998) 9–34.
[7] L. F. Coffin, Jr., A study of the effects of cyclic thermal stresses on a ductile metal, Transactions of the ASME 76 (1954) 931–950.
[8] O. H. Basquin, The exponential law of endurance tests, Proceedings of the American Society for Testing and Materials 10 (1910) 625–630.
[9] J. Morrow, Cyclic plastic strain energy and fatigue of metals, Internal Friction, Damping, and Cyclic Plasticity, ASTM STP 378 (1965) 45–87.

[10] T. DebRoy, H. L. Wei, J. S. Zuback, T. Mukherjee, J. W. Elmer, J. O. Milewski, A. M. Beese, A. Wilson-Heid, A. De, W. Zhang, Additive manufacturing of metallic components – process, structure and properties, Progress in Materials Science 92 (2018) 112–224.
[11] D. Herzog, V. Seyda, E. Wycisk, C. Emmelmann, Additive manufacturing of metals, Acta Materialia 117 (2016) 371–392.
[12] W. E. Frazier, Metal additive manufacturing: A review, Journal of Materials Engineering and Performance 23 (2014) 1917–1928.
[13] D. Tomus, Y. Tian, P. A. Rometsch, M. Heilmaier, X. Wu, Influence of post heat treatments on anisotropy of mechanical behaviour and microstructure of Hastelloy-X parts produced by selective laser melting, Materials Science and Engineering: A 711 (2018) 319–328.
[14] N. J. Harrison, I. Todd, K. Mumtaz, Reduction of micro-cracking in nickel superalloys processed by selective laser melting: A fundamental alloy design approach, Acta Materialia 94 (2015) 59–68.
[15] G. Marchese, E. Bassini, A. Aversa, M. Lombardi, D. Ugues, P. Fino, S. Biamino, Microstructural investigation of as-fabricated and heat-treated Inconel 625 and Inconel 718 fabricated by direct metal laser sintering, Materials Science and Engineering: A 797 (2020) 140155.
[16] R. Esmaeilizadeh, A. Keshavarzkermani, U. Ali, A. Pasha, H. Asgari, E. Toyserkani, Customizing mechanical properties of additively manufactured Hastelloy X parts by adjusting laser scanning speed, Journal of Alloys and Compounds 862 (2021) 158532.
[17] A. Keshavarzkermani, R. Esmaeilizadeh, U. Ali, P. D. Enrique, Y. Peng, A. Marvizi, T. Lucas, S. Shin, A. Hamed, E. Toyserkani, Controlling mechanical properties of additively manufactured Hastelloy X by altering solidification pattern during laser powder-bed fusion, Materials Science and Engineering: A 762 (2019) 138081.
[18] M. L. Montero-Sistiaga, Z. Liu, L. Bautmans, S. Nardone, G. Ji, J.-P. Kruth, J. Van Humbeeck, K. Vanmeensel, Effect of temperature on the microstructure and tensile properties of micro-crack free Hastelloy X produced by selective laser melting, Additive Manufacturing 31 (2020) 100893.
[19] N. Sanaei, A. Fatemi, Defects in additive manufactured metals and their effect on fatigue performance: A state-of-the-art review, Progress in Materials Science 117 (2021) 100724.
[20] A. Yadollahi, N. Shamsaei, Additive manufacturing of fatigue resistant materials: Challenges and opportunities, International Journal of Fatigue 98 (2017) 14–31.
[21] A. B. Spierings, T. L. Starr, K. Wegener, Fatigue performance of additive manufactured metallic parts, Rapid Prototyping Journal 19 (2013) 88–94.
[22] J. W. Pegues, N. Shamsaei, M. D. Roach, R. S. Williamson, Fatigue life estimation of additive manufactured parts in the as-built surface condition, Material Design and Processing Communications 1 (2019) e36.
[23] R. Shrestha, J. Simsiriwong, N. Shamsaei, Fatigue behavior of additive manufactured 316L stainless steel parts: Effects of layer orientation and surface roughness, Additive Manufacturing 28 (2019) 23–38.
[24] H. Gong, K. Rafi, H. Gu, G. D. Janaki Ram, T. Starr, B. Stucker, Influence of defects on mechanical properties of Ti-6Al-4V components produced by selective laser melting and electron beam melting, Materials and Design 86 (2015) 545–554.
[25] S. Tammas-Williams, P. J. Withers, I. Todd, P. B. Prangnell, The influence of porosity on fatigue crack initiation in additively manufactured titanium components, Scientific Reports 7 (2017) 7308.
[26] C. M. Pilgar, J.-L. Bouvard, T. Fixy, D. Pino-Munoz, A generic tomography-based conforming finite elements model, Finite Elements in Analysis and Design 253 (2026) 104472.
[27] Y. Murakami, Metal Fatigue: Effects of Small Defects and Nonmetallic Inclusions, Elsevier, 2002.
[28] S. Romano, A. Brückner-Foit, A. Brandão, J. Gumpinger, T. Ghidini, S. Beretta, Fatigue properties of AlSi10Mg obtained by additive manufacturing: Defect-based modelling and prediction of fatigue strength, International Journal of Fatigue 117 (2018) 28–40.
[29] Y. Kok, X. Tan, P. Wang, M. L. S. Nai, N. H. Loh, E. Liu, S. B. Tor, Anisotropy and heterogeneity of microstructure and mechanical properties in metal additive manufacturing: A critical review, Materials and Design 139 (2018) 565–586.
[30] B. E. Carroll, T. A. Palmer, A. M. Beese, Anisotropic tensile behavior of Ti-6Al-4V components fabricated with directed energy deposition additive manufacturing, Acta Materialia 87 (2015) 309–320.
[31] S. Beretta, S. Romano, A comparison of fatigue strength sensitivity to defects for materials manufactured by AM or traditional processes, International Journal of Fatigue 94 (2017) 178–191.
[32] T. Wang, S. Dai, H. Liao, H. Zhu, Fatigue behavior of Hastelloy X superalloy fabricated by selective laser melting, Materials Science and Engineering: A 833 (2022) 142561.
[33] D. L. McDowell, F. P. E. Dunne, Microstructure-sensitive computational modeling of fatigue crack formation, International Journal of Fatigue 32 (2010) 1521–1542.
[34] C. M. Pilgar, A. M. Fernandez, S. Lucarini, J. Segurado, Effect of printing direction and thickness on the mechanical behavior of slm fabricated hastelloy-x, International Journal of Plasticity 153 (2022) 103250.
[35] W. D. Pilkey, D. F. Pilkey, Z. Bi, Peterson's Stress Concentration Factors, 4th ed., John Wiley and Sons, 2020.
[36] J. N. Goodier, Concentration of stress around spherical and cylindrical inclusions and flaws, Journal of Applied Mechanics 1 (1933) 39–44.
[37] A. L. Gurson, Continuum theory of ductile rupture by void nucleation and growth: Part I, Journal of Engineering Materials and Technology 99 (1977) 2–15.
[38] V. Tvergaard, A. Needleman, Analysis of the cup-cone fracture in a round tensile bar, Acta Metallurgica 32 (1984) 157–169.
[39] H. Luong, A. Vinogradov, Fatigue life estimation of additively manufactured metallic materials: A short review, Fatigue and Fracture of Engineering Materials and Structures 45 (2022) 3476–3497.
[40] Z. Zhan, H. Li, Machine learning based fatigue life prediction with effects of additive manufacturing process parameters for printed SS 316L, International Journal of Fatigue 142 (2021) 105941.
[41] H. Bao, S. Wu, Z. Wu, G. Kang, X. Peng, P. J. Withers, A machine-learning fatigue life prediction approach of additively manufactured metals, Engineering Fracture Mechanics 242 (2021) 107508.
[42] A. Agrawal, A. Choudhary, A fatigue strength predictor for steels using ensemble data mining, Proceedings of the 25th ACM International on Conference on Information and Knowledge Management (2014) 2497–2500.

[43] T. Lookman, P. V. Balachandran, D. Xue, R. Yuan, Active learning in materials science with emphasis on adaptive sampling using uncertainties for targeted design, npj Computational Materials 5 (2019) 21.
[44] C. E. Rasmussen, C. K. I. Williams, Gaussian Processes for Machine Learning, MIT Press, 2006.
[45] B. Settles, Active learning, Synthesis Lectures on Artificial Intelligence and Machine Learning 6 (2012) 1–114.
[46] Y. S. Lee, et al., Process optimization and microstructure of lpbf hastelloy x, Metals (2023).
[47] M. L. Montero-Sistiaga, Z. Liu, L. Bautmans, S. Nardone, G. Ji, J.-P. Kruth, J. Van Humbeeck, K. Vanmeensel, Effect of temperature on the microstructure and tensile properties of micro-crack free hastelloy x produced by selective laser melting, Additive Manufacturing 31 (2020) 100995.
[48] C. M. Pilgar, A. M. Fernandez, J. Segurado, A fatigue life model accounting for the combined effect of surface roughness and microstructure: Application to slm fabricated hastelloy-x, International Journal of Fatigue 184 (2024) 108298.
[49] J. Kangazian, et al., Additive manufacturing of hastelloy x ni-based alloy, Transactions of the Indian Institute of Metals (2025).
[50] R. P. Skelton, D. Gandy, Creep–fatigue damage accumulation and life prediction methods, Materials at High Temperatures (2008).
[51] S. S. Manson, Behavior of materials under conditions of thermal stress, Technical Report NACA TN 2933, National Advisory Committee for Aeronautics, 1953.
[52] R. E. Peterson, Notch sensitivity, in: G. Sines, J. L. Waisman (Eds.), Metal Fatigue, McGraw-Hill, 1959, pp. 293–306.
[53] H. Neuber, Theory of stress concentration for shear-strained prismatical bodies with arbitrary nonlinear stress-strain law, Journal of Applied Mechanics 28 (1961) 544–550.
[54] D. Arola, C. L. Williams, Estimating the fatigue stress concentration factor of machined surfaces, International Journal of Fatigue 24 (2002) 923–930.
[55] J. Chaboche, Time-independent constitutive theories for cyclic plasticity, International Journal of Plasticity 2 (1986) 149–188.
[56] J. Lemaitre, J. L. Chaboche, Mechanics of Solid Materials, Cambridge University Press, Cambridge, 1990.
[57] R. Cunningham, A. Nicolas, J. Madsen, E. Fodran, E. Anagnostou, M. D. Sangid, A. D. Rollett, Analyzing the effects of powder and post-processing on porosity and properties of electron beam melted ti-6al-4v, Materials Research Letters 5 (2017) 516–525.